The Astrophysical Journal, 910:115 (33pp), 2021 April 1 https://doi.org/10.3847/1538-4357/abe1c8

High Metal Content of Highly Accreting Quasars

Marzena Śniegowska[1,2], Paola Marziani[3], Bożena Czerny[2], Swayamtrupta Panda[1,2], Mary Loli Martínez-Aldama[2], Ascensión del Olmo[4], and Mauro D'Onofrio[5]
[1] Nicolaus Copernicus Astronomical Center, Polish Academy of Sciences, Bartycka 18, 00-716 Warsaw, Poland; msniegowska@camk.edu.pl
[2] Center for Theoretical Physics, Polish Academy of Sciences, Al. Lotników 32/46, 02-668 Warsaw, Poland
[3] Istituto Nazionale di Astrofisica (INAF), Osservatorio Astronomico di Padova, I-35122 Padova, Italy
[4] Instituto de Astrofísica de Andalucía (IAA- CSIC), Glorieta de Astronomía, E-18080 Granada, Spain
[5] Dipartmento di Fisica & Astronomia, Università di Padova, Padova, Italy
Received 2020 September 28; revised 2021 January 13; accepted 2021 January 26; published 2021 April 2

Abstract

We present an analysis of UV spectra of 13 quasars believed to belong to extreme Population A (xA) quasars, aimed at the estimation of the chemical abundances of the broad-line-emitting gas. Metallicity estimates for the broad-line-emitting gas of quasars are subject to a number of caveats; xA sources with the strongest Fe II emission offer several advantages with respect to the quasar general population, as their optical and UV emission lines can be interpreted as the sum of a low-ionization component roughly at quasar rest frame (from virialized gas), plus a blueshifted excess (a disk wind), in different physical conditions. Capitalizing on these results, we analyze the component at rest frame and the blueshifted one, exploiting the dependence of several intensity line ratios on metallicity Z. We find that the validity of intensity line ratios as metallicity indicators depends on the physical conditions. We apply the measured diagnostic ratios to estimate the physical properties of sources such as density, ionization, and metallicity of the gas. Our results confirm that the two regions (the low-ionization component and the blueshifted excess) of different dynamical conditions also show different physical conditions and suggest metallicity values that are high, and probably the highest along the quasar main sequence, with $Z \sim 20-50\ Z_{\odot}$, if the solar abundance ratios can be assumed constant. We found some evidence of an overabundance of aluminum with respect to carbon, possibly due to selective enrichment of the broad-line-emitting gas by supernova ejecta.

Unified Astronomy Thesaurus concepts: Quasars (1319); Active galactic nuclei (16); Radio quiet quasars (1354)

1. Introduction

Thanks to large public databases such as the Sloan Digital Sky Survey (SDSS), we have unrestricted access to a large wealth of astronomical data (e.g., several editions of quasar catalogs, Schneider et al. 2010; Pâris et al. 2017; and of value-added measurements by Shen et al. 2011). SDSS spectra of high-redshift quasars ($z \gtrsim 2$) cover the rest-frame UV spectral range. It has been known since the 1970s that measurements of UV emission lines can be used to explore the physical and chemical properties of active galactic nuclei (AGNs). Landmark papers provided the basic understanding of line formation processes due to photoionization (e.g., Davidson & Netzer 1979; Wills & Netzer 1979; Baldwin et al. 2003).

The chemical composition of the line-emitting gas is an especially intriguing problem from the point of view of the evolution of cosmic structures, but also from the technical side. Nagao et al. (2006b) investigated BLR metallicities using various emission-line flux ratios and claimed that the typical metallicity of the gas in that region is at least supersolar, with typical $Z \sim 5\ Z_{\odot}$. Moreover, studies of metallicity–redshift dependence (Nagao et al. 2006b; Juarez et al. 2009) show a lack of metallicity evolution up to $z \approx 5$. Similar results are obtained for Nagao et al. (2006a). The highest-redshift quasars ($z \gtrsim 5$; e.g., Bañados et al. 2016; Nardini et al. 2019) are known to show UV spectra remarkably similar to the ones observed at low redshift, especially the ones accreting at a high rate and radiating at high Eddington ratio (Diamond-Stanic et al. 2009; Plotkin et al. 2015; Sulentic et al. 2017).[6] Perhaps surprisingly, these sources are suspected to have high metal content in their line-emitting gas, due to the consistent values of several diagnostic ratios measured in quasars with similar spectral properties at low and high z (Martínez-Aldama et al. 2018a), and indicating highly supersolar metal content.

Several techniques are applied to estimate the chemical composition in Galactic nebulae (see, e.g., Feibelman & Aller 1987 for planetary nebulae). Classical techniques used for H II and other nebulae (including the narrow-line regions (NLRs)) are unfortunately not applicable to the broad-line regions of quasars. Permitted and intercombination lines are too broad to resolve fine-structure components of doublets; line profiles are composites and may originate in regions that are spatially unresolved, and unresolved or only partially resolved in radial velocity as well.

However, quasar emission-line profiles still offer important clues in the radial velocity domain. The shape of the profile is strongly dependent on the ionization potential of the ionic species from which the line is emitted: it is expedient to subdivide the broad lines in low- and high-ionization lines (LILs and HILs). The LIL group in the spectral range under analysis (1200–2000 Å) includes the following lines: Si II λ1263, Si II λ1814, Al II λ1671, Al III λ1860, Si III] λ1892, and C III] λ1909. High-ionization lines are N IV] λ1486, O IV] λ1402, C IV λ1549, Si IV λ1397, O III] λ1663, and He II λ1640 (for detailed discussion see Collin-Souffrin & Lasota 1988; Collin-Souffrin et al. 1988; Gaskell 2000). The Al III, Si III], and C III] lines are sometimes referred to as "intermediate-ionization lines": even if they are mainly produced within the fully ionized region of the emitting gas clouds (Negrete et al. 2012), the ionization potential of their

[6] The effect is most likely due to a bias: for a flux-limited sample, the highest radiators at a given black hole mass are the ones that remain detectable at highest z (Sulentic et al. 2014).

ionic species is closer to the ones of the LILs, and typically $\lesssim$20 eV.

Not only do the two groups of lines (HILs and LILs) show different kinematic properties (Sulentic et al. 1995), but their emission is also likely to occur in fundamentally different physical conditions (Marziani et al. 2010). The HILs are characterized also by the evidence of strong blueshifted emission, very evident in C IV (e.g., Sulentic et al. 2007; Richards et al. 2011; Coatman et al. 2016). Therefore, a careful line comparison/decomposition is necessary, lest inferences may be associated with a nonexistent region with inexplicable properties.

The interpretation of two line components involves a virialized region, of relatively low ionization (hereafter referred to as the virialized, low-ionization BLR associated with a symmetric broad component (BC)), possibly including emission from the accretion disk, and a region of higher ionization, associated with a disk wind or a clumpy outflow, a scenario first proposed by Collin-Souffrin et al. (1988) and further developed by Elvis (2000), and observationally supported by reverberation mapping (e.g., Peterson & Wandel 1999) and the apparent lack of correlation between HILs and LILs in luminous quasars (e.g., Mejía-Restrepo et al. 2016; Sulentic et al. 2017). Even if all lines were emitted by a wind (Murray et al. 1995; Murray & Chiang 1997; Proga 2007a), the conditions at the base of the wind may strongly differ from the ones downstream in the outflow.

While each UV metal line contains information related to composition (Hamann & Ferland 1992), not all of the lines listed above can be used in practice. For instance, the N V and Si II λ1263 lines are strongly affected by blending with Lyα; other lines, such as Si II λ1814 and N IV] λ1486, are usually weak and require high signal-to-noise ratio (S/N) to be properly measured. The choice of diagnostic ratios used for metallicity estimates will be a compromise between S/N, easiness of deblending, and straightforwardness of physical interpretation. In practice, apart from Lyα, only the strongest broad features will be considered as potential metallicity estimators in this work (Section 3). The ratio (Si IV + O IV])/C IV has been widely used in past studies (Hamann & Ferland 1999 and references therein); this ratio is relatively easy to measure and seems to be the most stable ratio against distribution of gas densities and ionization parameter in the BLR (Nagao et al. 2006b). The ratios involving N V λ1240, like N V/C IV, are sensitive to ionization parameter and to nitrogen abundance (e.g., Dietrich et al. 2003; Wang et al. 2012a). We will rediscuss the use of these ratios in the context of the xA quasar spectral properties (Section 5.8).

Both physical conditions and chemical abundances vary along the quasar main sequence (see, e.g., Sulentic et al. 2000b; Kuraszkiewicz et al. 2009; Shen & Ho 2014; Wildy et al. 2019; Panda et al. 2020b). Solar and even slightly subsolar values are possible toward the extreme Population B, where Fe II emission is often undetectable above noise (e.g., Hamann et al. 2002; Punsly et al. 2018). At the other extreme, where Fe II is most prominent, estimates suggest $Z \gtrsim 10\ Z_{\odot}$ (Panda et al. 2018, 2019). Baldwin et al. (2003) derived $Z \approx 15\ Z_{\odot}$, although in the particular case of "nitrogen-loud" quasars. Apart from the extremes, it is not obvious whether there is a continuous systematic trend along the sequence. Previous estimates consistently suggest supersolar metallicity up to $Z \lesssim 10\ Z_{\odot}$ (Warner et al. 2004). Other landmark studies consistently found supersolar metallicity: Hamann & Ferland (1992) derived Z up to $\lesssim$15 $Z_{\odot}$; Nagao et al. (2006b) found typical values $Z \approx 5\ Z_{\odot}$, with $Z \sim 10\ Z_{\odot}$ for the most luminous quasars from the (Si IV + O IV])/C IV ratio. Sulentic et al. (2014) inferred a large dispersion with the largest value in excess of 10 $Z_{\odot}$. Similar results were reached by Shin et al. (2013), whose Si IV + O IV]/C IV ratio measurements suggested $Z \gtrsim 10\ Z_{\odot}$.

Most interesting along the quasar main sequence are the high accretors. They are selected according to empirical criteria (e.g., Wang et al. 2013, 2014; Marziani & Sulentic 2014; Du et al. 2016b) and defined by having $R_{\rm Fe\ II} > 1$, that is, with the Fe II λ4570 blend on the blue side of Hβ (as defined by Boroson & Green 1992) flux exceeding the flux of Hβ. In the optical diagram of the quasar main sequence (Sulentic et al. 2000b; Shen & Ho 2014) they are at the extreme tip in terms of Fe II prominence and identified as extreme Population A (hereafter xA), following Sulentic et al. (2002). Depending on redshift, we look for high accretors using different criteria. In the case of $z \gtrsim 1$, it is expedient to use a criterion based on two UV line intensity ratios:

1. Al III/Si III] > 0.5,
2. C III]/Si III] < 1.0,

following Marziani & Sulentic (2014). These criteria are met by the sources identified as the xA population by Sulentic and collaborators. xA quasars are radiating at the highest luminosity per unit mass, and at low z they are characterized by relatively low black hole masses for their luminosities and high Eddington ratios (Mathur 2000; Sulentic et al. 2000a). There is evidence that xA sources tend to have high metallicity (Shemmer et al. 2004; Martínez-Aldama et al. 2018a). Similar properties have been identified as characteristic of narrow-line Seyfert 1 galaxies (NLSy1s) with strong Fe II emission. NLS1s also have unusually high metallicities for their luminosities. Shemmer & Netzer (2002) have shown that NLSy1s deviate significantly from the nominal relationship between metallicity and luminosity in AGNs. As several studies distinguish between NLSy1s and "broader-lined" AGNs, we remark here that all Fe II-strong NLSy1s meeting the selection criterion $R_{\rm Fe\ II} > 1$ are extreme Population A sources.[7]

The aim of this work is to investigate the metallicity-sensitive diagnostic ratios of the UV spectral range for extreme Population A quasars, i.e., for highly accreting quasars. Section 2 defines our sample and provides some basic information. In Section 3 we define the diagnostic ratios and describe the basic observational results. In Section 4 we compare measured diagnostic ratios and compare them with the ones obtained from photoionization simulations. In Section 5 we discuss our results in terms of method caveats, metal enrichment, accretion parameters, and their implications on the nature of xA sources. We show the UV spectra in Appendix A (Figure 16), along with the multicomponent fit analysis of the emission blends, and in Appendix B we show the trend of Z-sensitive ratios as a function of ionization parameter, density, and metallicity.

[7] NLSy1s are identified by the line width of the Hβ BC being FWHM(H$\beta_{\rm BC}$) $\leqslant$ 2000 km s^{-1} (Osterbrock & Pogge 1985), Population A sources are identified by FWHM(H$\beta_{\rm BC}$) $\leqslant$ 4000 km s^{-1} (Sulentic et al. 2000a). Imposing a fixed limit on line FWHM, although very convenient observationally, has no direct physical meaning, and its interpretation might be sample dependent. See Marziani et al. (2018) for a discussion of the issue.

2. Sample

2.1. Sample Definition

Qualitatively, extreme Population A objects show prominent Al III and weak or absent C III] emission lines. In general, they show low emission-line equivalent widths ($\approx\frac{1}{2}$ of them meet the W(C IV) $\lesssim 10$ Å and qualify as weak-lined quasars following Diamond-Stanic et al. 2009)[8] and a spectrum that is easily recognizable even by a visual inspection, also because of the "trapezoidal" shape of the C IV profile and the intensity of the λ1400 blend, comparable to the one of C IV (Martinez-Aldama et al. 2018b).

xA sources were selected according to the criteria given in Section 1, using line measurements automatically obtained by the `splot` task with a cursor script within the IRAF data reduction package. We focus on the spectral range from ≈1200 to 2100 Å, where (1) UV lines used for xA identification are present and (2) the strongest emission features helpful for metallicity diagnostics are also located. The Lyα + N V blend is usually too heavily compromised by absorptions, which make it impossible to reconstruct the emission components especially for Lyα. We will make some consideration on the mean strength of the N V with respect to C IV and He II λ1640 (Section 5.3), but we will not consider N V as a diagnostic. We selected SDSS DR12[9] spectra in the redshift range $2.15 < z < 2.40$, relatively bright ($r < 19$) to ensure moderate to high S/N in the continua (in all cases S/N $\gtrsim 5$ in the continuum, and the wide majority with S/N $\gtrsim 10$), and of low decl. $\delta < 10$. The redshift range was chosen to allow for the possibility of Hβ coverage in the H band by eventual near-IR spectroscopic observations. The DR12 sample selected with these criteria is ≈500 sources strong. xA sources were selected out of this sample with an automated procedure, inspected to avoid broad absorption lines, and further vetted for obtaining a small pilot sample of ∼10 sources. A larger sample of xA sources will be considered in a subsequent work (K. Garnica et al. 2021, in preparation). The final selection includes 13 sources. With the adopted selection criteria in flux and redshift, we expect a small dispersion in the accretion parameters (especially luminosity; Section 5.2). Indeed, the selected sources are rather homogeneous in terms of spectral appearance, with a few sources included in our sample that, however, show borderline criteria. They will be considered in Section 4.1.1 in terms of their individual U, $n_{\rm H}$.

2.2. Sample Properties

Table 1 provides basic information for the 13 sources of our sample: SDSS name, redshift from the SDSS, the difference between our redshift estimation using Al III (described in 3.1) and the SDSS redshift $\delta z = z - z_{\rm SDSS}$, the g-band magnitude provided by Adelman-McCarthy et al. (2008), the $g - r$ color index, the rest-frame-specific continuum flux at 1700 and 1350 Å measured on the rest frame, and the S/N at 1450 Å. All other sources were covered by FIRST (Becker et al. 1995) but undetected. Considering that the typical rms scatter of FIRST radio maps is ≈0.15 Jy, as well as the typical fluxes in the g band, we have upper limits $\lesssim$5 in the radio-to-optical ratio, qualifying the sample sources as radio-quiet. Distances were computed using the formula provided by Sulentic et al. (2006, their Equation (B.5)), and ΛCDM cosmology ($\Omega_\Lambda = 0.7$, $\Omega_{\rm M} = 0.3$, $H_0 = 70$ km s^{-1} Mpc^{-1}). The bolometric luminosity is $\sim 10^{47}$ erg s^{-1}, assuming a bolometric correction B.C.$_{1350} =$ 3.5 (Richards et al. 2006). The sample rms is just ≈0.2 dex: all sources are in a narrow range of distances and have observed fluxes within a factor of ≈2 from their average. This is, in principle, an advantage for the estimation of the physical parameters such as $L/L_{\rm Edd}$, considering the large uncertainty and serious biases associated with the estimation of $M_{\rm BH}$ from UV high-ionization lines. Accretion parameters will be discussed in Section 5.2.

3. Methods

3.1. Redshift Determination

The estimate of the quasar systemic redshift in the UV is not trivial, as there are no low-ionization narrow lines available in the spectral range (Vanden Berk et al. 2001). In practice, one can resort to the broad LIL. Negrete et al. (2014) and Martínez-Aldama et al. (2018a) consider the Si II λ1263 and O I λ1302 lines to obtain a first estimate. A readjustment is then made from the wavelength of the Al III doublet, which is found, in almost all cases, to have a consistent redshift. To determine the Al III shift, those authors used multicomponent fits with all the lines in the region of the blend λ1900 included. The peak of Al III is clearly visible in the spectra of our sample, since in high accretors emission of Al III is strong with respect to the other lines in the blend at 1900 Å. We decided to use only this method for redshift estimation (in Table 1), and to measure the peak, we use single Gaussian fitting from the `splot` task of the Al III doublet and/or of the Si III] line, depending on which feature is sharper. The obtained values are usually $\geqslant z_{\rm SDSS}$ (Table 1). This is not a surprise, as $z_{\rm SDSS}$ is based on lines that are mainly blueshifted in xA sources and hence is a systematic underestimation of the unbiased redshift.

3.2. Diagnostic Ratios Sensitive to U, Density, Z

Line ratios are sensitive to different parameters. In the UV range, four groups of diagnostic ratios are defined in the literature (e.g., Negrete et al. 2012; Martinez-Aldama et al. 2018b):

1. C IV/Si IV + O IV] and C IV/He II have been widely applied as metallicity indicators (e.g., Shin et al. 2013). In principle, C IV/He II and Si IV/He II should be sensitive to C and Si abundance because the He abundance relative to hydrogen can be considered constant. The ionization potentials of C^{2+} and He^{+} are similar. The main difference is that the He II line is a recombination line, equivalent to H I Hα, and the regions where they are formed are not coincident (see Figure 4).
2. Ratios involving N V, N V/C IV, and N V/He II have been also widely used in past work, after it was noted that the N V line was stronger than expected in a photoionization scenario (e.g., Osmer & Smith 1976). A selective enhancement of nitrogen (Shields 1976) is expected owing to secondary production of N by massive and intermediate-mass stars, yielding [N/H] $\propto Z^2$ (Vila-Costas & Edmunds 1993; Izotov & Thuan 1999).

[8] Weak-lined quasars are mostly xA sources, judging from their location along the main sequence (Marziani et al. 2016a) and that the limit at $W \approx 10$ Å separates the low-W side of a continuous distribution of the xA C IV equivalent width peaked right at around 10 Å (Martínez-Aldama et al. 2018a).

[9] https://www.sdss.org/dr12/

Table 1
Source Identification and Basic Properties

SDSS NAME (1)	z_{SDSS} (2)	δz (3)	g (4)	$g-r$ (5)	f_λ(1700 Å) (6)	f_λ(1350 Å) (7)	S/N (8)
J010657.94−085500.1	2.355	0.006	18.18	0.095	662	951	20
J082936.30+080140.6	2.189	0.008	18.366	0.302	672	939	11
J084525.84+072222.3	2.269	0.017	18.204	0.331	668	989	13
J084719.12+094323.4	2.295	0.004	18.940	0.234	368	511	17
J085856.00+015219.4	2.160	0.002	17.916	0.255	709	1204	21
J092641.41+013506.6	2.181	0.004	18.591	0.337	377	670	21
J094637.83−012411.5	2.212	0.002	18.561	0.178	385	595	18
J102421.32+024520.2	2.319	0.008	18.49	0.177	478	694	23
J102606.67+011459.0	2.253	0.003	18.982	0.206	428	525	13
J114557.84+080029.0	2.338	0.009	18.545	0.369	243	360	5
J150959.16+074450.1	2.255	0.008	18.938	0.278	223	346	9
J151929.45+072328.7	2.394	0.008	18.662	0.171	405	507	19
J211651.48+044123.7	2.352	0.000	18.825	0.220	404	573	32

Note. Column (1): SDSS coordinate name. Column (2): SDSS redshift. Column (3): correction to redshift estimated in the present work ($\delta z = z - z_{SDSS}$). Column (4): g-band magnitude from Adelman-McCarthy et al. (2008). Column (5): color index $g-r$. Column (6): continuum flux measured at 1700 Å in units of 10^{-17} erg s^{-1} cm^{-2} Å^{-1}. Column (7): continuum flux measured at 1350 Å in the same units. Column (8): S/N measured at continuum level at 1450 Å.

This process might be especially important at the high metallicities inferred for the quasar BLR. Therefore, estimates based on N V may differ in a systematic way from estimates based on other metal lines (e.g., Matsuoka et al. 2011). In the present sample of quasars, contamination by narrow and semibroad absorption is severe, and even if we model precisely the high-ionization lines, it might be impossible to reconstruct the unabsorbed profile of the red wing of Lyα. In addition, S/N is not sufficient to allow for a careful measurement of N IV] λ1486 and N III] λ1750 lines. We defer the systematic analysis of nitrogen lines to a subsequent work, while discussing the consistency of the N V measures in a high-Z scenario (Section 5.3).

3. The ratios Al III/Si III] and Si III]/C III] are sensitive to density, as the ratios involve intercombination lines with a well-defined critical density ($n_c \sim 10^{10}$ cm^{-3} for C III], Hamann et al. 2002; $n_c \sim 10^{11}$ cm^{-3} for Si III], Negrete et al. 2010).
4. Si III]/Si IV, Si II λ1814/Si III], and Si II λ1814/Si IV are sensitive to the ionization parameters and insensitive to Z, as they are different ionic species of the same element.

Other intensity ratios entail a dependence on metallicity Z, but also on ionization parameter U and density n_H (Marziani et al. 2020).

3.3. Line Interpretation and Diagnostic Ratios

The comparison between LILs and HILs has provided insightful information over a broad range of redshift and luminosity (Corbin & Boroson 1996; Marziani et al. 1996, 2010; Shen 2016; Bisogni et al. 2017; Sulentic et al. 2017; Vietri et al. 2018). An LIL BLR appears to remain basically virialized (Marziani et al. 2009; Sulentic et al. 2017), as the Hβ profile remains (almost) symmetric and unshifted with respect to rest frame even if C IV blueshifts can reach several thousands of kilometers per second. In Population A, the lines have been decomposed into two components:

1. The BC, also known as the intermediate component, the core component, or the central BC following various authors (e.g., Brotherton et al. 1994; Popović et al. 2002; Kovačević-Dojčinović et al. 2015; Adhikari et al. 2016). The BC is modeled by a symmetric and unshifted profile (Lorentzian for Population A; Véron-Cetty et al. 2001; Sulentic et al. 2002; Zhou et al. 2006) and is believed to be associated with a virialized BLR subsystem.
2. The blueshifted component (BLUE). A strong blue excess in Population A C IV profiles is obvious, as in some C IV profiles—like the one of the xA prototype I Zw 1 or high-luminosity quasars—BLUE dominates the total emission-line flux (Marziani et al. 1996; Leighly & Moore 2004; Sulentic et al. 2017). For BLUE, there is no evidence of a regular profile, and the fit attempts to empirically reproduce the observed excess emission. BLUE is detected in an LIL such as Hβ at a very low level and is not strongly affecting FWHM measurements (Negrete et al. 2018).

3.3.1. Broad Component

Diagnostic ratios are not equally well measurable for the BC and the BLUE. For the BC, the following constraints and caveats apply:

C IV/, Si IV/, Al III/ over He II.—He II is weak but measurable in most of the objects. Ratios such as C IV/He II λ1640, Si IV/He II λ1640, and Al III/He II λ1640 (U dependent) offer Z indicators. Especially for the low-ionization conditions of the BC emitting gas, these ratios are well behaved (Sections 3.5 and 3.6) and will form the basis of the Z estimates presented in this paper.

Si IV/C IV.—There are problems in estimating the Si IV line intensity: an overestimation might be possible because of difficult continuum placement (see, e.g., the case of SDSS J085856.00+015219.4 in Appendix A). The relative contribution of Si IV to the blend at 1400 Å is unclear (Wills & Netzer 1979). A strong BC contribution of O IV] is unlikely, as this line has a critical density $n_c \sim 10^{10}$ cm^{-3} (Zheng 1988; see also the isophotal contour of Si IV/O IV] in Appendix B). Our measurements are nonetheless compared to Si IV + total O IV] CLOUDY prediction.

Al III/Si III].—This ratio is sensitive to density in the low-ionization BLR domain (Negrete et al. 2012). Values Al III/Si III] > 1 are possible if density is higher than 10^{11} cm^{-3}, the critical density of Si III]. We will not use this parameter as a metallicity estimator, although, in principle, for fixed physical conditions (setting $n_{\rm H}$ and U) the Al III/Si III] and Si III]/C III] ratios may become dependent mainly on electron temperature and so on metallicity (Section 3.5). The ratio of the total emission in the λ1900 blend Al III+Si III]+C III] over C IV has been used as a metallicity estimator (Sulentic et al. 2014). Considering the uncertain contribution of Fe III emission and especially of the Fe III λ1914 line in the xA spectra, we will not use the total intensity of the λ1900 blend as a diagnostic.

C IV/Al III.—Biases might be associated with the estimate of the C IV $\lambda1549_{\rm BC}$, especially when BLUE is so prominent that C IV $\lambda1549_{\rm BC}$ contributes to a minority fraction.

3.3.2. BLUE Component

C IV/He II λ1640.—The He II λ1640 BLUE is well visible merging smoothly with the red wing of C IV. The ratio C IV/He II λ1640 might be affected by the decomposition of the blend, leading to an overestimate of the He II emission. This ratio is in principle sensitive to metallicity. However, the increase is not monotonic at relatively high U (see the panel for C IV/He II λ1640 in Figure 2). The resulting effect is that the C IV/He II λ1640 ratio within the uncertainties leaves the Z unconstrained between 0.1 and 100 solar.

C IV/(O IV] + Si IV).—The blueshifted excess at 1400 Å is ascribed to O IV + Si IV emission. A significant contribution can be associated with O IV], and several transitions of O IV that are computed by CLOUDY (see, e.g., Keenan et al. 2002) are especially relevant at high U values and moderately low $n_{\rm H}$ ($\sim 10^8$ cm^{-3}). The blue side of the line is relatively straightforward to measure for computing C IV/λ1400 with a multicomponent fit, although difficult continuum placement, narrow absorption lines, and blending on the blue side make it difficult to obtain a very precise measurement. A total λ1400 BLUE emission exceeding C IV is possible if, assuming $\log U \gtrsim 0$, $\log n_{\rm H} \gtrsim 9$ [cm^{-3}], the metallicity value is very high, $20\ Z_\odot \lesssim Z \lesssim 100\ Z_\odot$ (Section 3.6).

(O IV]+Si IV)/He II λ1640.—By the same token, the He II λ1640 overestimation may lead to a lower (O IV]+Si IV)/He II λ1640 ratio.

3.4. Analysis via Multicomponent Fits

We analyze 13 objects using the `specfit` task from IRAF (Kriss 1994). The use of the χ^2 minimization is aimed at providing a heuristic separation between the BC and the blue component (BLUE) of the emission lines. After redshift correction following the method described in Section 3.1, for each source of our sample we perform a detailed modeling using various components as described below, including computation of asymmetric errors (Section 3.4.1). As mentioned in Section 3.2, in our analysis we consider five diagnostic ratios for the BC, C IV/λ1400, C IV/He II λ1640, Al III/He II λ1640, λ1400/He II λ1640, and λ1400/Al III, and three for the BLUE, C IV/λ1400, C IV/He II λ1640, and λ1400/He II λ1640. The C IV/He II λ1640 is used with care, as it may yield poor constraints. In addition, it is important to stress that, of the five ratios measured on the BC, only three (the ones dividing by the intensity of He II λ1640 BC) are independent. We compare the fit results with arrays of CLOUDY (Ferland et al. 2013) simulations for various metallicities and physical conditions (Section 3.5).

For each source we perform the multicomponent fitting in three ranges described below. The best fit is identified by the model with the lowest χ^2, i.e., with a minimized difference between the observed and the model spectrum. Following the data analysis by Negrete et al. (2012), we use the following components:

The continuum.—This was modeled as a power law, and we use the line-free windows around 1300 and 1700 Å (two small ranges where there are no strong emission lines) to scale it. If needed, we divide the continuum into three parts (corresponding to the three regions mentioned below). Assumed continua are shown in the figures of Appendix A.

Fe II *emission.*—This usually does not contribute significantly in the studied spectral ranges. We consider the Fe II template that is based on CLOUDY simulations of Brühweiler & Verner (2008) when necessary. In practice, the contamination by the blended Fe II emission yielding a pseudo-continuum is negligible. Some Fe II emission lines were detectable in only a few objects and around ≈1715 Å, at 1785 Å, and at 2020 Å. In these cases, we model them using single Gaussians.

Fe III *emission.*—This affects more the λ1900 region and seems to be strong when Al III λ1860 is strong as well (Hartig & Baldwin 1986). To model these lines, we use the template of Vestergaard & Wilkes (2001).

Region 1300–1450 Å.—This is dominated by the Si IV + O IV] high-ionization blend with strong blueshifted component. Fainter lines such as Si II λ1306, O I λ1304, and C II λ1335 are also detectable. For the broad and blueshifted components we use the same model as in the case of C IV and He II λ1640. This spectral range is often strongly affected by absorption.

Region 1450–1700 Å.—This is dominated by the C IV emission line, which we model as fixed in the rest-frame wavelength Lorentzian profile representing the BC, and two blueshifted asymmetric Gaussian profiles vary freely. The same model is used for He II λ1640.

Region 1700–2200 Å is dominated by Al III, Si III], and Fe III intermediate-ionization lines. We model Al III and Si III] using Lorentzian profiles, following Negrete et al. (2012). C III] emission is also included in the fit, although the dominant contribution around 1900 Å is to be ascribed to Fe III (Martínez-Aldama et al. 2018a and references therein). We use the template of Vestergaard & Wilkes (2001) to model Fe III emission. No BLUE is ascribed to these intermediate-ionization lines.

Absorption lines.—These are modeled by Gaussians and included whenever necessary to obtain a good fit.

The fits to the observed spectral ranges are shown in the figures of Appendix A.

3.4.1. Error Estimation on Line Fluxes

The choice of the continuum placement is the main source of uncertainty in the measurement of the emission-line intensities. The fits in Appendix A show that, in the majority of cases, the FWHMs of the Al III and Si III] lines (assumed equal) satisfy the condition FWHM(Al III) ∼ FWHM(C IV$_{\rm BC}$ ∼ FWHM(Si IV$_{\rm BC}$). Figure 1 shows the best-fit, maximum, and minimum placement of the continuum, which we choose empirically. With this approach the continua of Figure 1 should provide the continuum uncertainty at a $\pm 3\sigma$ confidence.

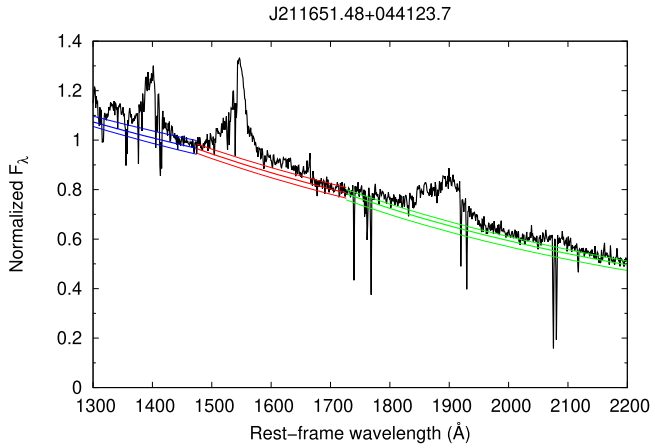

Figure 1. Continuum estimation for J211651.48+044123.7 from our sample. Range 1300–1450 Å is shown in blue, 1450–1700 Å in red, and 1750–2200 Å in green. The continuum lines in each range represent from the top: the maximum, the best-fit, and the minimum continuum placement.

The continuum placement strongly affects the measurement of an extended feature such as the Fe III blends and the He II λ1640 emission. Figure 1 makes it evident that errors on fluxes are asymmetric. The thick line shows the continuum best fit and the thinner minimum and maximum plausible continua. Even if the minimum and maximum are displaced by the same difference in the intensity with respect to the best-fit continuum, assuming the minimum continuum would yield an increase in line flux larger than the flux decrease assuming the maximum continuum level. In other words, a symmetric uncertainty in the continuum-specific flux translates into an asymmetric uncertainty in the line fluxes. To manage asymmetric uncertainties, we assume that the distribution of errors follows the triangular distribution (D' Agostini 2003). This method assumes linear decreasing on either side of maximum of the distribution (which is the best fit in our case) to the values obtained for maximum and minimum contributions of the continuum. We motivate using the triangular error distribution as a relatively easy analytical method to deal with asymmetric errors. For each line measurement we calculate the variance using the following formula for the triangular distribution:

$$\sigma^2(X) = \frac{\Delta^2 x_+ + \Delta^2 x_- + \Delta x_+ + \Delta x_-}{18}, \quad (1)$$

where Δx_+ and Δx_- are differences between measurement with maximum and best continuum and measurement with best and minimum continuum, respectively. To analyze the error of diagnostic ratios, we propagate uncertainties using standard formulas of error propagation.

3.5. Photoionization Modeling

To interpret our fitting results, we compare the line intensity ratio for BC and BLUE with the ones predicted by CLOUDY 13.05 and 17.02 simulations (Ferland et al. 2013, 2017).[10] An array of simulations is used as reference for comparison with the observed line intensity ratios. It was computed under the assumption that (1) column density is $N_c = 10^{23}$ cm^{-2}; (2) the continuum is represented by the model continuum of Mathews & Ferland (1987), which is believed to be appropriate for Population A quasars; and (3) microturbulence is negligible. The simulation arrays cover the hydrogen density range $7.00 \leqslant \log(n_H) \leqslant 14.00$ and the ionization parameter $-4.5 \leqslant \log(U) \leqslant 1.00$, in intervals of 0.25 dex. They are repeated for values of metallicities in a range encompassing five orders of magnitude: 0.01, 0.1, 1, 2, 5, 10, 20, 50, 100, 200, 500, and 1000 $Z_\odot$. Extremely high metallicity $Z \gtrsim 100\ Z_\odot$ is considered physically unrealistic ($Z \approx 100\ Z_\odot$ implies that more than half of the gas mass is made up by metals!), unless the enrichment is provided in situ within the disk (Cantiello et al. 2020). The behavior of diagnostic line ratios as a function of U and n_H for selected values of Z is shown in Figure 17 of Appendix B.

3.5.1. Basic Interpretation

The line emissivity ϵ_{coll} (ergs cm^{-3} s^{-1}) of a collisionally excited line emitted from an element X in its ith ionization stage has a strong temperature dependence. In the high-density limit

$$\epsilon_{X^i,coll} = n_{X^i,l}\beta A_{X^i,ul} h\nu_0 \frac{g_{X^i,l}}{g_{X^i,u}} \exp\left(-\frac{h\nu_0}{kT_e}\right) \propto n_{X^i,l} \exp\left(-\frac{h\nu_0}{kT_e}\right) \quad (2)$$

the line is said to be "thermalized," as its strength depends only on the atomic level population and not on the transition strength (Hamann & Ferland 1999). β is the photon escape probability, and $A_{X^i,ul}$ is the spontaneous decay coefficient. At low densities we have

$$\epsilon_{X^i,coll} = n_{X^i,l} n_e q_{X^i,lu} h\nu_0 \propto n_{X^i}^2 T_e^{-1/2} \exp\left(-\frac{h\nu_0}{kT_e}\right). \quad (3)$$

The recombination lines considered in our analysis are Hβ and He II λ1640, for which the emissivity (with an approximate dependence of radiative recombination coefficient α on electron temperature; Osterbrock & Ferland 2006) becomes

$$\epsilon_{Y^j,rec} = n_{Y^j}\, n_e\, \alpha\, h\nu_0 \propto n_{Y^j}^2 T_e^{-1}, \quad (4)$$

and n_{Y^j} is the number density of the parent ion.

Under these simplifying, illustrative assumptions we can write

$$\frac{\epsilon_{X^i,coll}}{\epsilon_{Y^j,rec}} \propto \left(\frac{n_{X^i}}{n_{Y^j}}\right)^2 T_e^{\frac{1}{2}} \exp\left(-\frac{h\nu_0}{kT_e}\right) \quad (5)$$

for the low-density case and

$$\frac{\epsilon_{X^i,coll}}{\epsilon_{Y^j,rec}} \propto \frac{n_{X^i}}{n_{Y^j}^2} T_e \exp\left(-\frac{h\nu_0}{kT_e}\right) \quad (6)$$

for the high-density case.

Similarly, for the ratio of two collisionally excited lines at frequencies ν_0 and ν_1,

$$\frac{\epsilon_{X^i,coll}}{\epsilon_{Y^j,coll}} \propto \left(\frac{n_{X^i}}{n_{Y^j}}\right)^\kappa \exp\left(-\frac{h(\nu_0 - \nu_1)}{kT_e}\right), \quad (7)$$

[10] The arrays were computed over several years with CLOUDY 13.05, in large part before CLOUDY 17.02 became available. The computations with the two versions of the code are in agreement as far as the trends with U, n_H, and Z are concerned, although the derived Z values are a factor of ≈2 systematically lower with the 17.02 release of CLOUDY. In this paper we present the CLOUDY 17.02 for all estimates of metallicity and physical parameters U and n_H.

where $\kappa = 1$ and 2 in the high- and low-density case, respectively.

Connecting the relative chemical abundance to the line emissivity ratios in the previous equation requires the reconstruction of the ionic stage distribution for each element, i.e., the computation of the ionic equilibrium, as well as the consideration of the extension of the emitting region within the gas clouds, i.e., that the line emission is not cospatial, and possible differences in optical depth effects. This is achieved by the CLOUDY simulations. However, we can see that the main variable parameter for a given relative emissivity is T_e. In other words, electron temperature is the main parameter connected to metallicity. This is especially true for a fixed physical condition (U, n_H, $N_c = 10^{23}$, spectral energy distribution (SED) given). This is most likely the case for xA sources: the spectral similarity implies that the scatter in physical properties is modest. We further investigate this issue in Section 4.3.

The electron temperature is also the dominating factor affecting the strength of the He II λ1640 line, for a given density. The He II Lyα line at 304 Å ionizes hydrogen atoms and other ionic species with ionization potential up to 3 ryd. Being absorbed by different ionic species, He II λ1640 Lyα cannot sustain a population of excited electrons at the level $n = 2$ of He II λ1640. This is markedly different from hydrogen Lyα, which in case B is assumed to scatter many times and to sustain a population of hydrogen atoms at level $n = 2$. The He II line is therefore produced almost only by recombination, and no collisional excitation from level $n = 2$ or radiative transfer effects are expected, unlike the case of the hydrogen Balmer lines (Marziani et al. 2020). The prediction of the He II line is relatively simple once the electron temperature and the density are known by assumption or computation. The additional advantage in the use of He II is that there is no significant enhancement of the He abundance over the entire lifetime of the universe (Peimbert et al. 2001; Peimbert 2008). The normalization to the He II line flux of the flux of metal lines should yield robust Z estimates. This is shown by the isophotal contours of Appendix B (Figure 17), tracing the behavior of the diagnostic ratios as a function of Z and U: the (Si IV + O IV])/He II and Al III/He II ratios monotonically increase with Z over a large range of U; for C IV/He II λ1640 the behavior is monotonic at low U, but more complex at $\log U \sim -1 - 0$. Ratios involving pairs of metal lines yield more complex trends in the plane Z–U. At low n_H, the C IV/Al III ratio is a good Z estimator, although of limited usefulness since Al III is weak; at high n_H, its sensitivity is greatly reduced (Appendix B, Figure 17). The C IV/(Si IV + O IV]) does not appear to be especially sensitive to Z. The diagnostic ratios change as a function of Z, although the behavior as a function of n_H and U is roughly preserved (Appendix B, Figure 18).

3.6. Explorative Analysis of Photoionization Trends at Fixed Ionization Parameter and Density

One of the main results of previous investigations is the systematic differences in ionization between BLUE and BC (Marziani et al. 2010; Negrete et al. 2012; Sulentic et al. 2017). Previous inferences suggest very low ionization ($U \sim 10^{-2.5}$), also because of the relatively low C IV/Hβ ratio for the BC emitting part of the BLR, and high density. A robust lower limit to density $n_H \sim 10^{11.5}$ cm^{-3} has been obtained from the analysis of the Ca II triplet emission (Matsuoka et al. 2007; Panda et al. 2020a). Less constrained are the physical conditions for BLUE emission. Apart from C IV/H$\beta \gg 1$ and Lyα/Hβ and C IV/C III] also $\gg$1, few constraints exist on density and column density. This result hardly comes as a surprise considering the difference in dynamical status associated with the two components. It is expected that the BC is emitted in a region of high column density $\log N_c \gtrsim 23$ [cm^{-2}], not last because radiation forces are proportional to the inverse of N_c (Netzer & Marziani 2010, see also Ferland et al. 2009). More explicitly, the equation of motion for a gas cloud under the combined effect of gravitation and radiation forces contains an acceleration term due to radiation that is inversely proportional to N_c. The high-N_c region is expected to be relatively stable (at rest frame, with no sign of systematic, large shifts in Population A) and presumably devoid of low-density gas (considering the weakness of C III]; Negrete et al. 2012). The same cannot be assumed for BLUE. BLUE is associated with a high radial velocity outflow, probably with the outflowing streams creating BAL features when intercepted by the line of sight (e.g., Elvis 2000).

Here we consider $\log U = -2.5$, $\log n_H = 12$ (−2.5, 12), and $\log U = 0$, $\log n_H = 9$ (0, 9) as representative of the low- and high-ionization emitting gas. Figure 2 illustrates the behavior of the C IV/Hβ, He II λ1640/Hβ, and C IV/He II λ1640 in the high- and low-ionization cases as a function of metallicity. The C IV intensity with respect to Hβ has a steep drop around $Z \gtrsim 1\ Z_\odot$, after a steady increase for subsolar Z. The He II λ1640/Hβ ratio decreases steadily, with a steepening at around solar value. Physically, this behavior is due to the high value of the ionization parameter (assumed constant), while the electron temperature decreases with metallicity, implying a much lower collisional excitation rate for C IV production. The dominant effect for the He II λ1640 decrease is likely the "ionization competition" between C IV and He II λ1640 parent ionic species (Hamann & Ferland 1999). As a consequence, the ratio C IV/He II λ1640 has a nonmonotonic behavior with a local maximum around solar metallicity. At low ionization and high density, the behavior is more regular, as the steady increase in C IV/Hβ is followed by a saturation to a maximum C IV/Hβ. The He II λ1640/Hβ ratio is constant up to solar and steadily decreases above solar, where the ionization competition with triply ionized carbon sets on. The result is a smooth, steady increase in the C IV/He II λ1640 ratio.

Figure 3 shows the behavior of the other intensity ratios used as metallicity diagnostics, for BLUE and BC. Si IV + O IV]/C IV and Si IV + O IV]/He II λ1640 saturate above 100 $Z_\odot$. Only around $Z \sim 10\ Z_\odot$ are values C IV/Si IV + O IV] $\lesssim 1$ possible, but the behavior is not monotonic and the ratio rises again at $Z \gtrsim 30\ Z_\odot$, with the unpleasant consequence that a ratio C IV/Si IV + O IV] ≈ 1.6 might imply 10 $Z_\odot$ as well as 1000 $Z_\odot$. The ratios usable for the BC also show regular behavior. The C IV/Al III ratio remains almost constant up $Z \sim 0.1\ Z_\odot$, and then starts a regular decrease with increasing Z, due to the decrease of T_e with Z (C IV is affected more strongly than Al III). Interestingly, Al III/He II λ1640 shows the opposite trend, due to the steady decrease of the He II λ1640 prominence with Z. Especially of interest is, however, the behavior of ratio Al III/He II λ1640 that shows a monotonic, very linear behavior in the log-log diagram. As for the high-ionization case, values (Si IV + O IV])/C IV $\gtrsim 1$ are possible only at very high metallicity, although the nonmonotonic

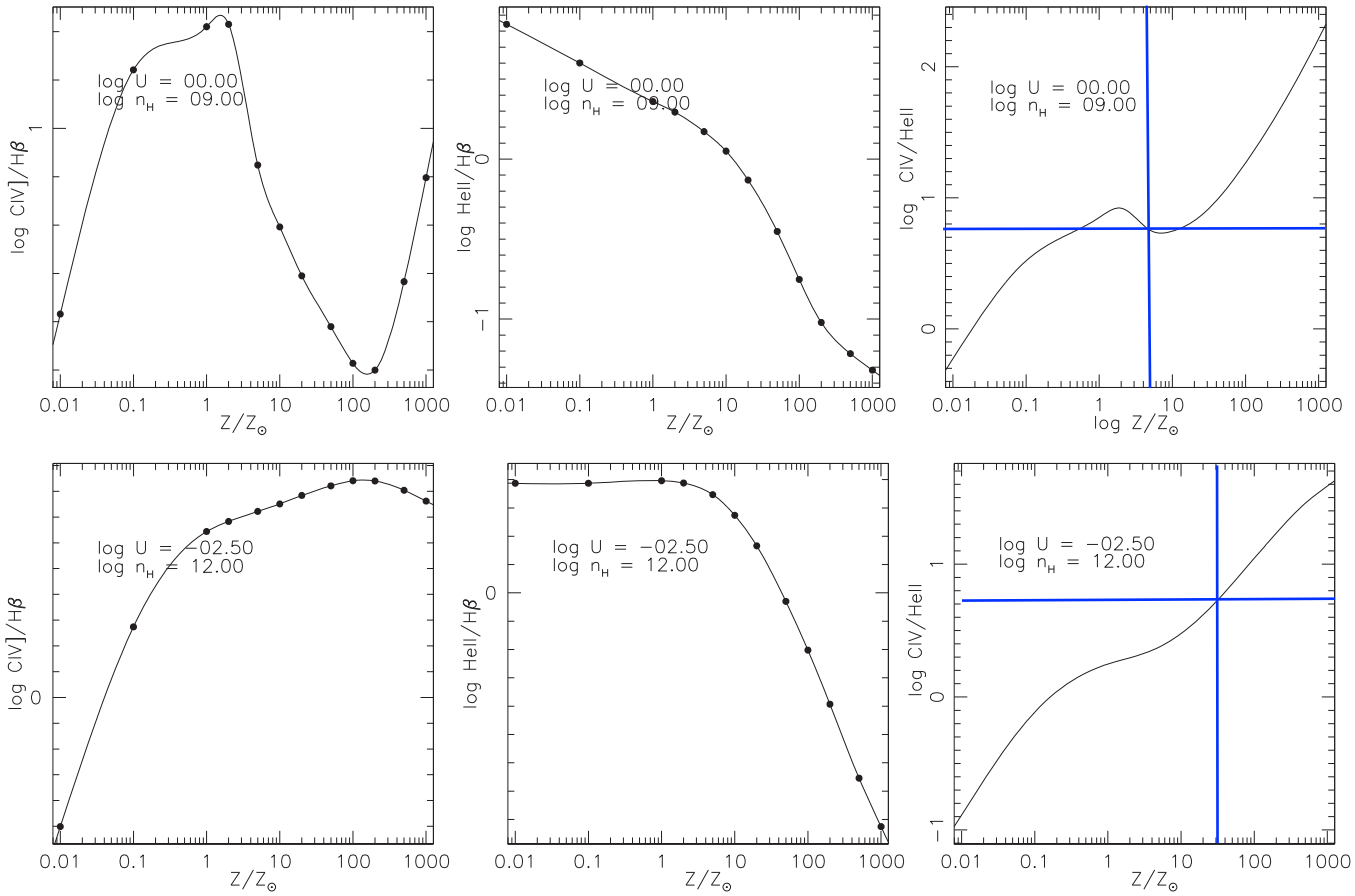

Figure 2. Computed intensity ratios involving C IV and He II λ1640 as a function of metallicity, for physical parameters U and $n_{\rm H}$ fixed: ($\log U$, $\log n_{\rm H}$) = (−1, 9) (top) and ($\log U$, $\log n_{\rm H}$) = (−2.5, 12) (bottom). Columns from left to right show C IV/Hβ, He II λ1640/Hβ, and C IV/He II λ1640.

behavior (around the minimum at $Z \approx 200\ Z_{\odot}$) complicates the interpretation of the observed emission-line ratios.

The ionization structure within the slab remains self-similar over a wide metallicity range, with the same systematic differences between the high- and low-ionization case (Figure 4), consistent with the assumption of a constant ionization parameter. As expected, the electron temperature decreases with metallicity, and the transition between the fully and partially ionized zone (FIZ and PIZ) occurs at smaller depth. In addition, close to the illuminated side of the cloud the electron temperature remains almost constant; the gas starts becoming colder before the transition from FIZ to PIZ. The depth at which $T_{\rm e}$ starts decreasing is well defined, and its value becomes lower with increasing Z (Figure 4). The effect is present for both the low- and high-ionization case, although it is more pronounced for the high-ionization case. Figure 5 shows how an increase in metallicity is affecting the $T_{\rm e}$ in the line-emitting cloud. Figure 5 reports the behavior of $T_{\rm e}$ at the illuminated face of the cloud ($\tau \sim 0$) and at maximum τ (corresponding to $N_{\rm c} = 10^{23}$ cm^{-2}, the side facing the observer) for the high- and low-ionization case. The $T_{\rm e}$ monotonically decreases as a function of metallicity. The difference between the two cloud faces is almost constant for the low-ionization case, with $\delta \log T_{\rm e} \approx 0.5$ dex, while it increases for the high-ionization case, reaching $\delta \log T_{\rm e} \approx 0.75$ dex at the highest Z value considered, $10^3\ Z_{\odot}$.

4. Results

4.1. Immediate Results

The observational results of our analysis involve the measurements of the intensity of the line BC and BLUE component separately. The rest-frame spectra with the continuum placements and the fits to the blends of the spectra are shown in Appendix A. Table 2 reports the measurement for the λ1900 blend. The columns list the SDSS identification code, the FWHM (in units of km s^{-1}) and equivalent width and flux of Al III (the sum of the doublet lines, in units of Å and 10^{-14} erg s^{-1} cm^{-2}, respectively), FWHM and flux of C III], and flux of Si III] (its FWHM is assumed equal to the one of the single Al III lines). Similarly, Table 3 reports the parameter of the C IV blend: equivalent width, FWHM and flux of the C IV BC, the flux of the C IV blueshifted component, and the fluxes of the BC and BLUE of He II λ1640. FWHM values are reported, but especially values $\gtrsim$5000 km s^{-1} should be considered as highly uncertain. There is the concrete possibility of an additional broadening ($\sim$10% of the observed FWHM) associated with nonvirial motions for the Al III line (A. del Olmo et al. 2021, in preparation). The fluxes of the BC and of BLUE of Si IV and O IV] are reported in Table 4. Intensity ratios with uncertainties are reported in Table 5. The last row lists the median values of the ratios with their semi-interquartile ranges (SIQR).

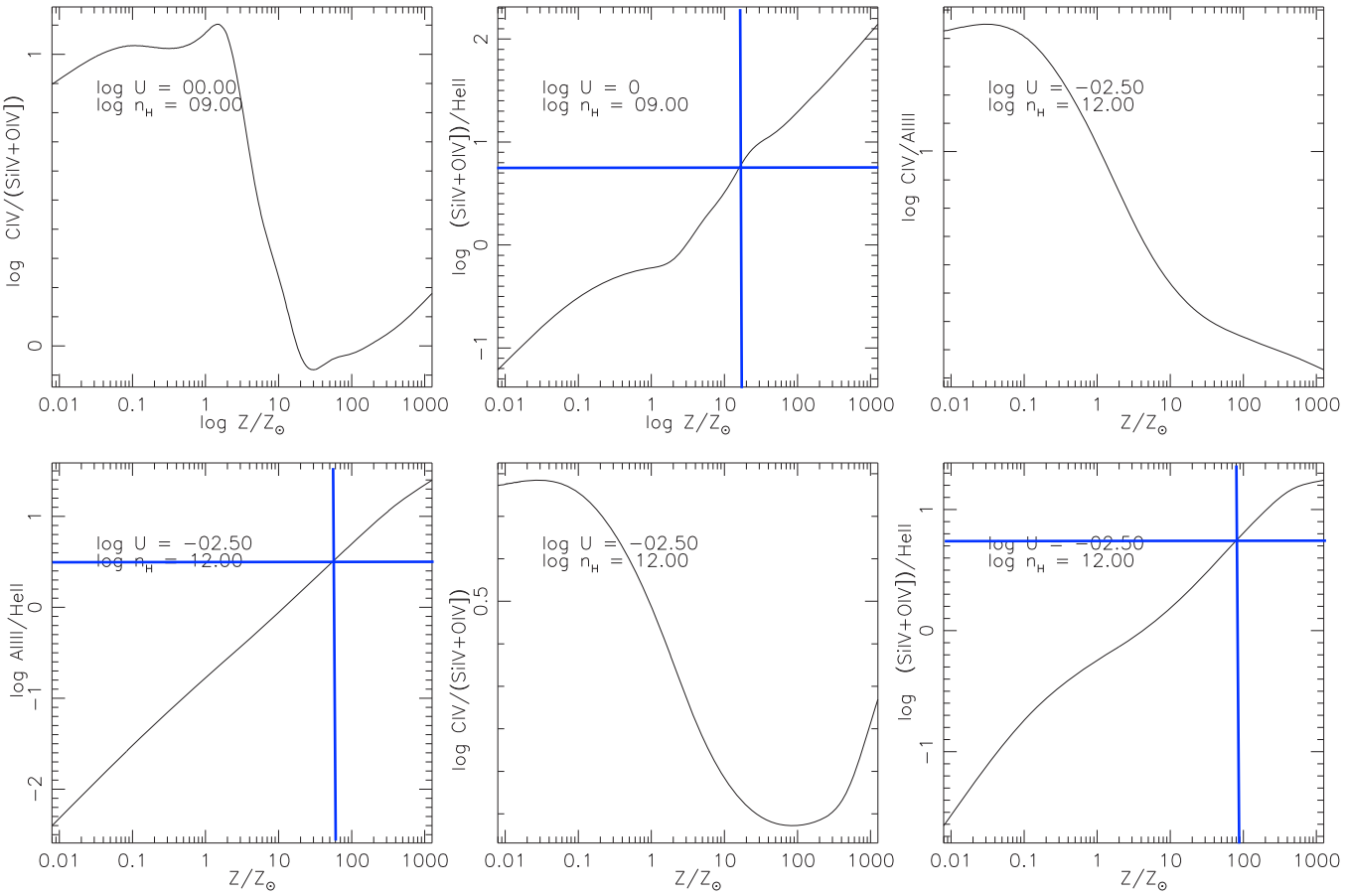

Figure 3. Behavior of the intensity ratios employed in this work (with the exception of C IV/He II λ1640 shown in the previous figure), as a function of metallicity, for physical parameters U and $n_{\rm H}$ fixed: ($\log U$, $\log n_{\rm H}$) = (−1, 9) and ($\log U$, $\log n_{\rm H}$) = (−2.5, 12). Top panels, from left to right: C IV/Si IV + O IV], (Si IV + O IV])/He II λ1640, C IV/Al III. Bottom panels, from left to right: Al III/He II λ1640, C IV/(Si IV + O IV]), (Si IV + O IV])/He II λ1640.

4.1.1. Identification of xA Sources and of "Intruders"

Figure 6 shows that the majority of sources meet both UV selection criteria and should be considered xA quasars. The median value of the Al III/Si III] (last row of Table 5) implies that the Al III is strong relative to Si III]. Also, Si III] is stronger than C III]. Both selection criteria are satisfied by the median ratios. Only one source (SDSS J084525.84+072222.3) shows C III]/Si III] significantly larger than 1. This quasar is, however, confirmed as an xA by the very large Al III/Si III], by the blueshift of C IV, and by the prominent λ1400 blend comparable to the C IV emission. The lines in the spectrum of SDSS J084525.84+072222.3 are broad, and any C III] emission is heavily blended with Fe III emission. The C III] value should be considered an upper limit. Three outlying/borderline data points (in orange) in Figure 6 have ratio C III]/Si III] $\sim$ 1, and Al III/Si III] consistent with the selection criteria within the uncertainties, but other criteria support their classification as xA. The borderline sources will be further discussed in Section 4.3. In conclusion, all 13 sources of the present sample save one should be considered bona fide xA sources.

It is intriguing that the intensity ratios C III]/Si III] and Al III/Si III] are apparently anticorrelated in Figure 6, if we exclude the two outlying points. Excluding the two outlying data points, the Spearman rank correlation coefficient is $\rho \approx 0.8$, which implies a 4σ significance for a correlation, but the correlation coefficient between the two ratios for the full sample is much lower. Given the small number of sources, a larger sample is needed to confirm the trend.

4.1.2. BC Intensity Ratios

Figure 7 shows the distribution of diagnostic intensity ratios C IV/He II λ1640, Si IV/He II λ1640, and Al III/He II λ1640 for the BC. The bottom panels of Figure 7 show the results for individual sources.

The vertical lines identify the median values, $\mu_{\frac{1}{2}}$(C IV/He II λ1640) $\approx$ 4.03, $\mu_{\frac{1}{2}}$(Al III/He II λ1640) $\approx$ 4.31, $\mu_{\frac{1}{2}}$(Si IV/He II λ1640) $\approx$ 6.39. The higher value for Si IV/He II λ1640 than for C IV/He II λ1640 implies $\mu_{\frac{1}{2}}$(C IV/Si IV) $\approx$ 0.69, a value that is predicted by CLOUDY for very low values of the ionization parameter (Appendix B). The C IV/Al III ratio is also constraining: the CLOUDY simulations indicate high Z and low ionization.

The distribution of the data points is relatively well behaved, with individual ratios showing small scatter around their median values. In the histogram, we see a tail made by three to five objects, suggesting systematically higher values. In particular, at least two objects (SDSS J102606.67+011459.0 and SDSS J085856.00+015219.4) show systematically higher ratios, with C IV/He II λ1640 $\approx$ 10, and Al III/He II λ1640 $\approx$ 4. Both of them show extreme C IV blueshifts, and SDSS J102606.67+011459.0 shows the highest Al III/Si III] ratio in the sample.

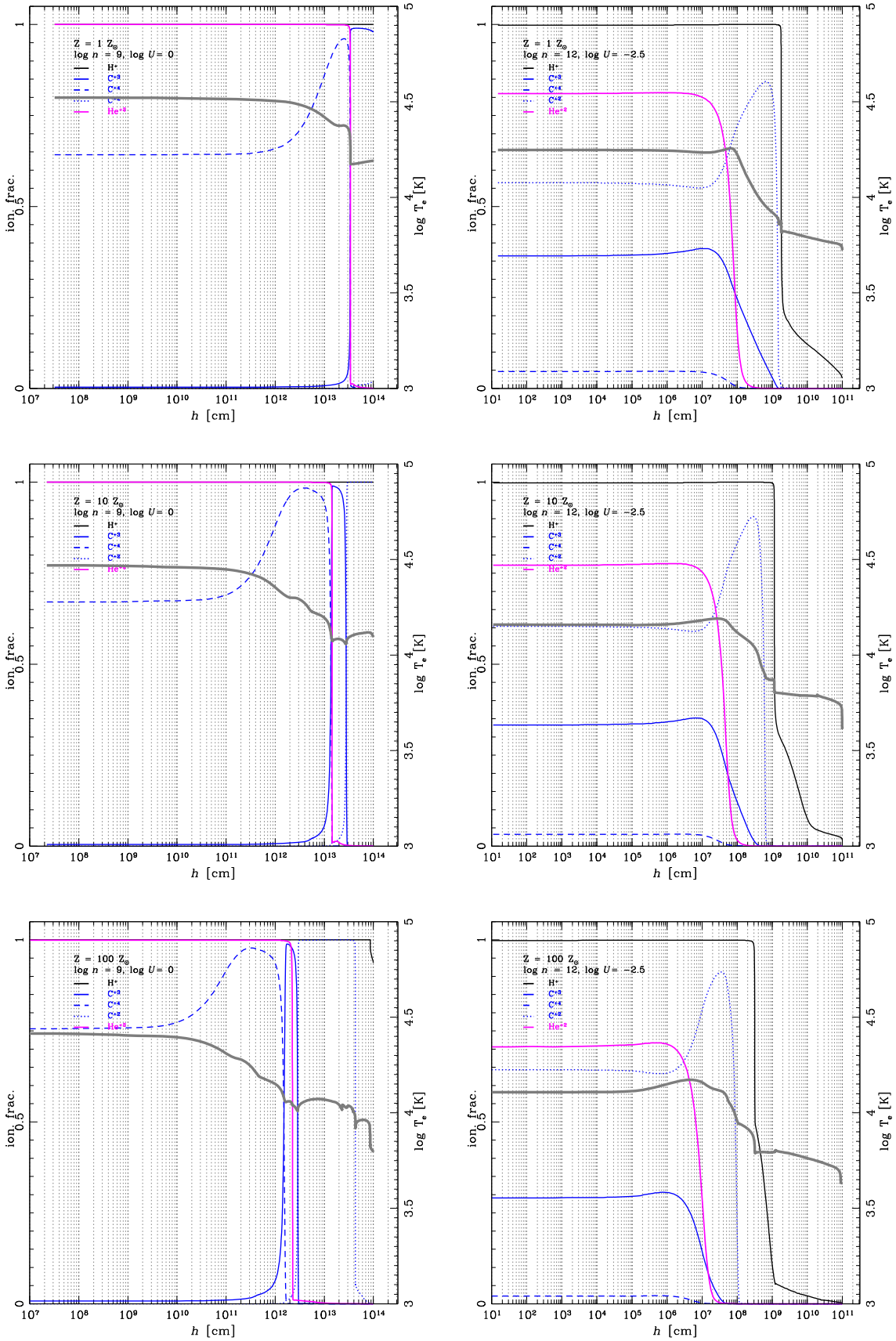

Figure 4. Ionization fraction and electron temperature (thick gray line) as a function of depth within the emitting gas slab, for physical parameters U and $n_{\rm H}$ fixed, computed with `CLOUDY 13.05`: ($\log U$, $\log n_{\rm H}$) = (−1, 9) (representative of BLUE and high-ionization case; left) and ($\log U$, $\log n_{\rm H}$) = (−2.5, 12) (representative of the low-ionization BLR; right), in order of increasing metallicity from top to bottom.

Table 2
Measurements in the λ1900 Blend Region

SDSS JCODE	Al III W	Al III FWHM	Al III Flux	C III] FWHM	C III] Flux	Si III] Flux
(1)	(2)	(3)	(4)	(5)	(6)	(7)
J010657.94−085500.1	7.9	5560	5.41 ± 0.38	6050	2.88 ± 0.14	7.2 ± 0.93
J082936.30+080140.6	10.2	5710	7.43 ± 0.42	5950	2.39 ± 0.21	4.85 ± 0.66
J084525.84+072222.3	13.1	5510	6.04 ± 0.52	5570	4.25 ± 0.53	3.13 ± 0.08
J084719.12+094323.4	9.9	5410	9.24 ± 0.24	5630	4.63 ± 0.36	5.61 ± 0.73
J085856.00+015219.4	7.7	5520	4.57 ± 0.37	5660	3.98 ± 0.12	4.39 ± 0.58
J092641.41+013506.6	8.0	5550	4.82 ± 0.3	5720	6.53 ± 0.23	5.48 ± 0.96
J094637.83−012411.5	5.0	2730	3.54 ± 0.24	2090	6.38 ± 0.22	5.1 ± 0.67
J102421.32+024520.2	10.1	5520	6.15 ± 0.31	6080	3.31 ± 0.2	5.1 ± 0.39
J102606.67+011459.0	9.5	5590	7.7 ± 0.35	5470	1.83 ± 0.33	3.64 ± 0.3
J114557.84+080029.0	11.4	5520	8.74 ± 0.38	6060	5.91 ± 0.83	6.3 ± 0.81
J150959.16+074450.1	11.8	5530	6.44 ± 0.53	6090	7.62 ± 0.25	7.58 ± 1.32
J151929.45+072328.7	10.5	5320	7.37 ± 0.51	5310	5.6 ± 0.62	7.16 ± 1.12
J211651.48+044123.7	6.1	5550	4.21 ± 0.4	5620	5.29 ± 0.2	5.35 ± 0.7

Note. Column (1): SDSS name. Columns (2) and (3): FWHM of Al III and C III] in km s^{-1}. Columns (4), (5), and (6): fluxes in units of 10^{-14} erg s^{-1} cm^{-2} for Al III, C III], and Si III].

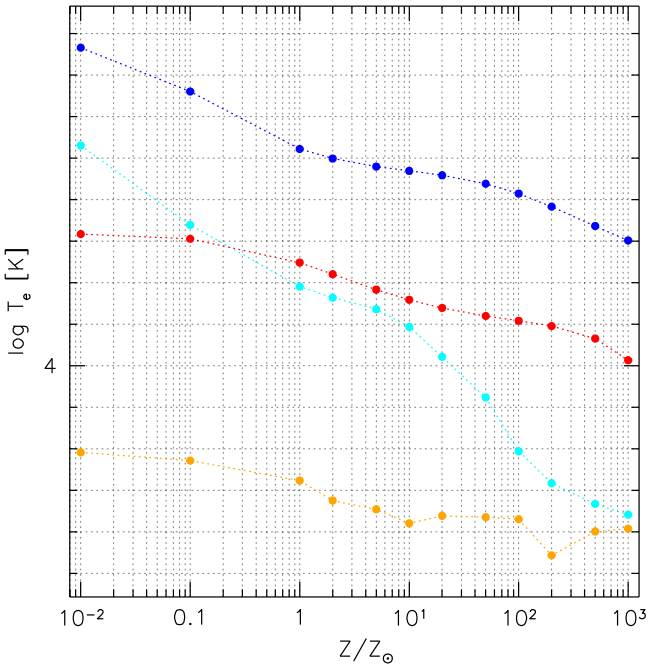

Figure 5. Electron temperature T_e as a function of metallicity Z, for physical parameters U and n_H fixed: (log U, log n_H) = (−1, 9) (representative of BLUE and high-ionization case; blue and cyan) and (log U, log n_H) = (−2.5,12) (representative of the low-ionization BLR; red and orange), from CLOUDY 13.05 computations. Blue and red refer to the first zone of the CLOUDY computation, i.e., to the illuminated surface of the clouds; cyan and orange, to the side of the cloud farther from the continuum sources, i.e., facing the observer.

Since the three ratios are, for fixed physical conditions, proportional to metallicity, we expect an overall consistency in their behavior, i.e., if one ratio is higher than the median for one object, also the other intensity ratios should be also higher. The lower diagrams are helpful to identify sources for which only one intensity ratio deviates significantly from the rest of the sample. A case in point is SDSS J082936.30+080140.6, whose ratio Al III/He II λ1640 ≈ 8 is one of the highest values, but whose C IV/He II λ1640 and Si IV/He II λ1640 are slightly below the median values. The fits of Appendix A show that this object is indeed extreme in Al III emission. The C IV and λ1400 blends are dominated by the BLUE excess, and an estimate of the C IV and Si IV BC is very difficult, as it accounts for a small fraction of the line emission. The He II λ1640 emission is almost undetectable, especially in correspondence with the rest frame. SDSS J082936.30+080140.6, along with other sources with high Al III/He II λ1640 or Si IV/He II λ1640 ratios, may indicate selective enhancement of aluminum or silicon (see also Section 5.7).

4.1.3. BLUE Intensity Ratios

Similar considerations apply to the blue intensity ratios. We see systematic trends in Figure 8 that imply consistency of the ratios for most sources, although the uncertainties are larger, especially for C IV/He II λ1640. The ratio C IV/(Si IV + O IV]) values are systematically higher than for the BC, while the C IV/He II λ1640 is slightly higher (median BLUE 5.8 vs. median BC 4.38). The ratio (Si IV + O IV])/He II λ1640 is much lower than for the BC (median BLUE 2.09 vs. median BC 6.27). The difference might be in part explained by the difficulty of deblending Si IV from O IV], and by the frequent occurrence of absorptions affecting the blue side of the blend. Both factors may conspire to depress BLUE. The bottom panels of Figure 8 are again helpful to identify sources for which intensity ratios deviate significantly from the rest of the sample. SDSS J102606.67+011459.0 shows a strong enhancement of C IV/He II λ1640 and Si IV + O IV], confirming the trend seen in its BC.

4.1.4. Correlation between Diagnostic Ratios

Figure 9 shows a matrix of correlation coefficients for all diagnostic ratios that we considered in this work. The 2σ confidence level of significance for the Spearman's rank correlation coefficient for 13 objects is achieved at $\rho \approx 0.54$. The highest degree of correlation is found between the ratios C IV/He II λ1640 and C IV/Si IV (0.87) and between C IV/He II λ1640 and Si IV/He II λ1640 (0.81). A milder degree of correlation is found between Al III/He II λ1640 and C IV/He II λ1640 (0.23) and Si IV/He II λ1640 (0.44). These results imply that Si IV and C IV are likely affected in a related way by a

Table 3
Measurements in the C IV Spectral Region

SDSS JCODE	C IV *W*	C IV BC FWHM	C IV BC Flux	C IV BLUE Flux	He II BC Flux	He II BLUE Flux
(1)	(2)	(3)	(4)	(5)	(6)	(7)
J010657.94−085500.1	18.6	5530	6.35 ± 1.04	13.46 ± 0.13	1.79 ± 0.46	1.93 ± 0.65
J082936.30+080140.6	15.5	3710 ± 670	1.83 ± 0.4	11.86 ± 0.03	0.8 ± 0.11	1.72 ± 0.69
J084525.84+072222.3	16.8	3760	5.04 ± 0.68	11.11 ± 0.21	1.06 ± 0.15	1.87 ± 0.81
J084719.12+094323.4	17.6	5520	11.53 ± 0.53	13.24 ± 0.07	2.14 ± 0.61	2.1 ± 1.19
J085856.00+015219.4	22.8	5460	9.84 ± 0.82	11.39 ± 0.09	0.65 ± 0.32	1.28 ± 0.48
J092641.41+013506.6	25.5	5550	7.79 ± 1.98	7.08 ± 0.08	1.94 ± 0.33	1.47 ± 0.39
J094637.83−012411.5	23.6	3670	15.63 ± 0.6	5.89 ± 0.09	1.87 ± 0.39	1.76 ± 0.7
J102421.32+024520.2	20.1	5640	6.74 ± 0.45	10.9 ± 0.08	1.9 ± 0.19	2.19 ± 1.07
J102606.67+011459.0	17.3	3700 ± 650	6.92 ± 1.22	12.23 ± 0.05	0.82 ± 0.34	1.15 ± 0.32
J114557.84+080029.0	18.4	3500 ± 700	6.84 ± 0.3	12.57 ± 0.03	2.01 ± 0.5	2.26 ± 1.02
J150959.16+074450.1	16.8	3530 ± 690	4.19 ± 0.84	9.73 ± 0.22	2.21 ± 0.14	1.48 ± 0.74
J151929.45+072328.7	19.4	3470 ± 590	5.47 ± 0.41	12.04 ± 0.16	1.52 ± 0.09	2.14 ± 0.24
J211651.48+044123.7	19.1	4750	13.04 ± 0.68	3.01 ± 0.24	0.99 ± 0.03	1.77 ± 0.69

Note. Column (1): SDSS name. Column (2): rest-frame equivalent width of the total C IV emission, i.e., C IV BLUE+BC, in Å. Column (3): FWHM of the C IV line in km s^{-1}. Columns (4) and (5): fluxes of the C IV BC and BLUE line. Columns (6) and (7): fluxes of the BC and BLUE components for the He II λ1640 line. All fluxes are in units of 10^{-14} erg s^{-1} cm^{-2}.

Table 4
Measurements in the λ1400 Region

SDSS JCODE	Si IV+O IV] BC FWHM	Si IV+O IV] BC Flux	Si IV+O IV] BLUE Flux
(1)	(2)	(3)	(4)
J010657.94−085500.1	5070	9.23 ± 1.4	6.24 ± 0.24
J082936.30+080140.6	5560	4.39 ± 0.81	7.3 ± 0.06
J084525.84+072222.3	5060	10.52 ± 0.58	2.69 ± 0.24
J084719.12+094323.4	5550	13.69 ± 0.86	3.79 ± 0.19
J085856.00+015219.4	6960	7.34 ± 0.69	8.55 ± 0.05
J092641.41+013506.6	5540	14.89 ± 0.45	4.05 ± 0.32
J094637.83−012411.5	4030	18.09 ± 0.7	3.29 ± 0.31
J102421.32+024520.2	5530	8.77 ± 0.64	4.06 ± 0.09
J102606.67+011459.0	5300	10.16 ± 0.57	4.01 ± 0.33
J114557.84+080029.0	3760	12.19 ± 1.22	5.71 ± 0.08
J150959.16+074450.1	3650	9.97 ± 0.75	5.86 ± 0.12
J151929.45+072328.7	3670	9.32 ± 1.05	4.48 ± 0.31
J211651.48+044123.7	4770	11.02 ± 0.77	0.81 ± 0.03

Note. Column (1): SDSS name. Column (2): FWHM of the Si IV line in km s^{-1}. Columns (3) and (4): fluxes of the BCs and the blue component line in units of 10^{-14} $ergs^{-1}$ cm^{-2}.

single parameter. The main parameter is expected to be T_e, and hence Z (Section 3.5.1). The Al III (normalized to the He II λ1640 flux) line shows much lower values of the correlation coefficient. The Al III line has a different dependence on U, n_H, and optical depth variations. The prominence of C III] with respect to Si III] decreases with Si IV/He II λ1640 BLUE, C IV/He II λ1640, and Si IV/He II λ1640 BLUE and increases with C IV/Si IV + O IV]. Apparently the C III]/Si III] ratio is strongly affected by an increase in metallicity and more in general by ratios that are indicative of "extremeness" in our sample. For BLUE, the two main independent Z estimators are correlated ($\rho \approx 0.68$).

4.2. Analysis of Z Distributions: Global Inferences on Sample

4.2.1. Fixed (U, n_H)

We propagated the diagnostic intensity ratios measured on the BC and BLUE components with their lower and upper uncertainties following the relation between ratios and Z in Figure 2, for the fixed physical conditions assumed in the low- and high-ionization region. The results are reported in Tables 6 and 7 for the BC and for the blueshifted component, respectively. The last row reports the median values of the individual sources' Z estimates with the sample SIQR. The distributions are shown in Figures 10 and 11, along with a graphical presentation of each source and its associated uncertainties.

Tables 6 and 7 permit us to quantify the systematic differences that are apparent in Figures 10 and 11. The agreement between the various estimators is good on average (the medians scatter around $\log Z \approx 1$ by less than 0.2 dex). However, there are systematic differences between the Z obtained from the various diagnostic ratios. Si IV and Al III over He II λ1640 apparently overestimate the Z by a factor of 2 with respect to C IV/He II λ1640. The out-of-scale values of C IV/Si IV and C IV/Al III may suggest that metallicity scaling according to solar proportion may not be strictly correct (Section 5.6). In the case of BLUE, several estimates

Table 5
Intensity Ratios for the BC and BLUE Line Components

SDSS JCODE	Al III/Si III] (BC)	C III]/Si III] (BC)	C IV/Si IV (BC)	C IV/He II λ1640 (BC)	Si IV/He II λ1640 (BC)	C IV/Al III (BC)	Al III/He II λ1640 (BC)	C IV/He II λ1640 (BLUE)	C IV/Si IV + O IV] (BLUE)	Si IV+ O IV]/ He II λ1640 (BLUE)
(1)	(2)	(3)	(4)	(5)	(6)	(7)	(8)	(9)	(10)	(11)
J010657.94−085500.1	0.75 ± 0.11	0.4 ± 0.05	0.69 ± 0.15	3.55 ± 1.09	5.16 ± 1.55	1.17 ± 0.21	3.02 ± 0.81	6.98 ± 3	2.16 ± 0.58	3.24 ± 1.1
J082936.30+080140.6	1.53 ± 0.23	0.49 ± 0.08	0.42 ± 0.12	2.29 ± 0.6	5.48 ± 1.26	0.25 ± 0.06	9.28 ± 1.39	6.89 ± 3.75	1.62 ± 0.6	4.24 ± 1.69
J084525.84+072222.3	1.93 ± 0.17	1.36 ± 0.17	0.48 ± 0.07	4.76 ± 0.92	9.95 ± 1.48	0.83 ± 0.13	5.71 ± 0.93	5.93 ± 3.07	4.13 ± 1.23	1.43 ± 0.63
J084719.12+094323.4	1.65 ± 0.22	0.82 ± 0.12	0.84 ± 0.07	5.38 ± 1.55	6.39 ± 1.86	1.25 ± 0.07	4.31 ± 1.23	6.29 ± 4.74	3.5 ± 1.75	1.8 ± 1.02
J085856.00+015219.4	1.04 ± 0.16	0.91 ± 0.12	1.34 ± 0.17	15.25 ± 7.63	11.38 ± 5.71	2.15 ± 0.25	7.08 ± 3.54	8.87 ± 5.01	1.33 ± 0.57	6.66 ± 2.47
J092641.41+013506.6	0.88 ± 0.16	1.19 ± 0.21	0.52 ± 0.13	4.03 ± 1.23	7.69 ± 1.31	1.62 ± 0.42	2.49 ± 0.45	4.83 ± 1.92	1.75 ± 0.53	2.76 ± 0.77
J094637.83−012411.5	0.7 ± 0.1	1.25 ± 0.17	0.86 ± 0.05	8.34 ± 1.74	9.66 ± 2.02	4.41 ± 0.35	1.89 ± 0.41	3.35 ± 1.99	1.79 ± 0.8	1.87 ± 0.77
J102421.32+024520.2	1.2 ± 0.11	0.65 ± 0.06	0.77 ± 0.08	3.55 ± 0.43	4.61 ± 0.58	1.1 ± 0.09	3.23 ± 0.37	4.97 ± 3.09	2.68 ± 1.04	1.85 ± 0.9
J102606.67+011459.0	2.12 ± 0.2	0.5 ± 0.1	0.68 ± 0.13	8.48 ± 3.83	12.46 ± 5.23	0.9 ± 0.16	9.45 ± 3.96	10.6 ± 4.21	3.05 ± 0.9	3.47 ± 1.01
J114557.84+080029.0	1.39 ± 0.19	0.94 ± 0.18	0.56 ± 0.06	3.41 ± 0.87	6.07 ± 1.64	0.78 ± 0.05	4.36 ± 1.11	5.56 ± 3.76	2.2 ± 1.11	2.53 ± 1.14
J150959.16+074450.1	0.85 ± 0.16	1 ± 0.18	0.42 ± 0.09	1.9 ± 0.4	4.51 ± 0.44	0.65 ± 0.14	2.92 ± 0.3	6.58 ± 4.49	1.66 ± 0.77	3.96 ± 1.98
J151929.45+072328.7	1.03 ± 0.18	0.78 ± 0.15	0.59 ± 0.08	3.61 ± 0.35	6.14 ± 0.79	0.74 ± 0.08	4.86 ± 0.45	5.62 ± 1.66	2.69 ± 0.76	2.09 ± 0.28
J211651.48+044123.7	0.79 ± 0.13	0.99 ± 0.13	1.18 ± 0.1	13.12 ± 0.78	11.08 ± 0.84	3.1 ± 0.34	4.23 ± 0.42	1.7 ± 0.73	3.71 ± 0.67	0.46 ± 0.18
Median	1.04 ± 0.34	0.91 ± 0.17	0.68 ± 0.16	4.03 ± 2.395	6.39 ± 2.23	1.10 ± 0.42	4.31 ± 1.35	5.93 ± 0.96	2.2 ± 0.65	2.53 ± 0.81

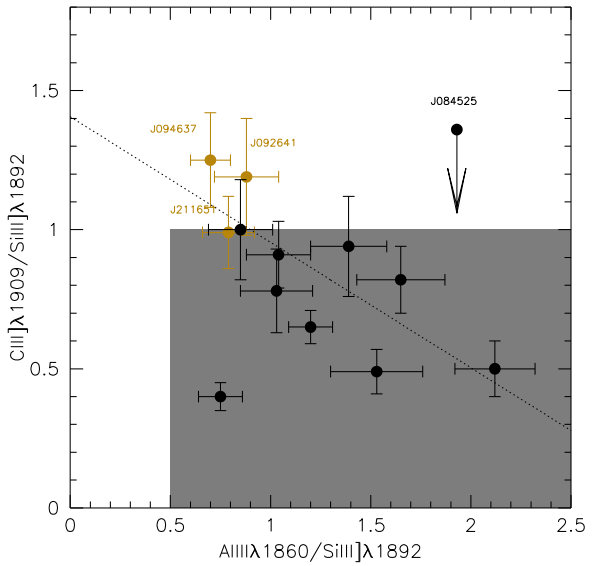

Figure 6. Relation between intensity ratios Al III λ1860/Si III] λ1892 and C III] λ1909/Si III] λ1892. The gray area corresponds to the parameter space occupied by the xA sources. Borderline sources are in orange color.

from C IV/He II λ1640 strongly deviate from the ones obtained with the other ratios, due to the nonmonotonic behavior of the relation between Z and C IV/He II λ1640, right in the range of metallicity that is expected. Figure 17 shows that the nonmonotonic behavior as a function of Z occurs for $-1 \lesssim \log U \lesssim 0$, assuming $\log n_{\rm H} = 9$.

The median values of all three ratios consistently suggest high metallicity with a firm lower limit $Z \approx 5$, and in the range $10\ Z_{\odot} \lesssim Z \lesssim 100\ Z_{\odot}$, with typical values between 20 and 50 $Z_{\odot}$. There is apparently a systematic difference between BC and BLUE, in the sense that Z derived from the BC is systematically higher than Z from BLUE. The difference is small in the case of C IV/He II λ1640 but is significant in the case of (Si IV + O IV])/He II λ1640, where Z from BLUE are a factor of 10 lower. We have stressed earlier that there are often absorptions affecting the BLUE of Si IV + O IV]/He II λ1640. Absorptions and the blending with C II λ1332 and Si IV BC lines make it difficult to properly define the continuum underlying the λ1400 blend at negative radial velocities. We think that the Si IV + O IV] BLUE intensity estimate is more of a lower limit. Another explanation might be related to the assumption of a constant density and U for all sources. While there are observational constraints supporting this condition for the BC (Panda et al. 2018, 2019, 2020b), there are no strong clues to the BLUE properties, save a high-ionization degree.

4.3. Z for Individual Sources for Fixed U, n_H

Table 8 reports the Z estimates for the BC, BLUE, and a combination of BC and BLUE for each individual object. The values reported are the median values of the individual objects' estimates from the different ratios. Here the Z value for each object is computed by vetting the ratios according to concordance. If the discordance is not due to a physical origin, but rather to instrumental problems (e.g., contamination by absorption lines, nonlinear dependence on Z of some ratios), a proper strategy is to use estimators such as the median that eliminate discordant values even for small sample sizes ($n \geqslant 3$). Measuring medians and SIQR is an efficient way to deal with the measurements of large samples of objects. All estimates $\log Z \lesssim 0$ were excluded, as either the product of heavy absorptions (Si IV + O IV]/He II λ1640) or the product of difficulties in relating the ratio (C IV/He II λ1640) to Z; apart from J211651.48+044123.7, the upper uncertainty of the negative estimates is so large that Z is actually unconstrained. The difference between BLUE and BC is even more evident: the median (last row) indicates a factor of $\approx$6 difference between BLUE and BC. The BC suggests a median $Z \approx 60\ Z_{\odot}$, while the BLUE $Z \approx 10\ Z_{\odot}$. The assumption that the wind and disk component have the same Z in each object is a reasonable one, with the caveats mentioned in Section 5.6. Therefore, the two estimates, for BLUE and BC, could be considered two independent estimators of Z. If the two estimates are combined for each individual object, $10\ Z_{\odot} \lesssim Z \lesssim 100\ Z_{\odot}$, with a median value of $Z \approx 20\ Z_{\odot}$.

There is a good agreement between the Z median estimates from the BC and BLUE of C IV, $\log Z \approx 1.27$ versus $\log Z \approx 1.13$, respectively (Tables 6 and 7). Ignoring Si IV +O IV] and Al III, the $Z \approx 20\ Z_{\odot}$ value derived for the C IV BC is not affected by a possible enhancement of [Si/C] and [Al/C] with respect to the solar values. If the carbon abundance is used as a reference, the BC Z estimate from Al III and Si IV could point toward a selective enhancement of Si and Al with respect to C.

The disagreement between BLUE and BC Z estimates rests on the blueshifted component of Si IV + O IV]. The disagreement between the Z estimates from ratios involving Si IV +O IV] BC and BLUE might be explained if one considers that the measurement of the Si IV+O IV] BLUE is most problematic and the Si IV+O IV] intensity might be systematically underestimated.

4.4. Estimates of Z Relaxing the Constraints on U and n_H

We computed the χ^2 in the following form, to identify the value of the metallicity for median values of the diagnostic ratios and for the diagnostic ratios of individual objects relaxing the assumption of fixed density and ionization parameters. For each object k, and for each component c, we can write

$$\chi^2_{\rm kc}(n_{\rm H}, U, Z) = \sum_{\rm i} w_{\rm ci} \left(\frac{R_{\rm kci} - R_{\rm kci,mod}(n_{\rm H}, U, Z)}{\delta R_{\rm kci}} \right)^2, \quad (8)$$

where the summation is done over the available diagnostic ratios, and the χ^2 is computed with respect to the results of the CLOUDY simulations as a function of U, $n_{\rm H}$, and Z (subscript "mod"). Weights $w_{\rm ci} = 1$ were assigned to C IV/He II λ1640, Si IV/He II λ1640, and Al III/He II λ1640; $w_{\rm ci} = 0$ or 0.5 was assigned to C IV/Al III and C IV/Si IV. For BLUE, the three diagnostic ratios were all assigned $w_{\rm ci} = 1$. The Z estimates for the BC are based on the three ratios involving He II λ1640 normalization.

To gain a global, bird's-eye view of the Z dependence on the physical parameters, Figure 12 shows the 3D space U, $n_{\rm H}$, Z. Each point in this space corresponds to an element of the grid of CLOUDY in the parameter space and is consistent with the minimum χ^2 within the uncertainties at 1σ confidence level. The case shown in the panels of Figure 12 is the one with the median values of the sample objects.

The distribution of the data points is constrained in a relatively narrow range of U, $n_{\rm H}$, Z, at very high density, low ionization, and high metallicity. Within the limit in U, $n_{\rm H}$, the

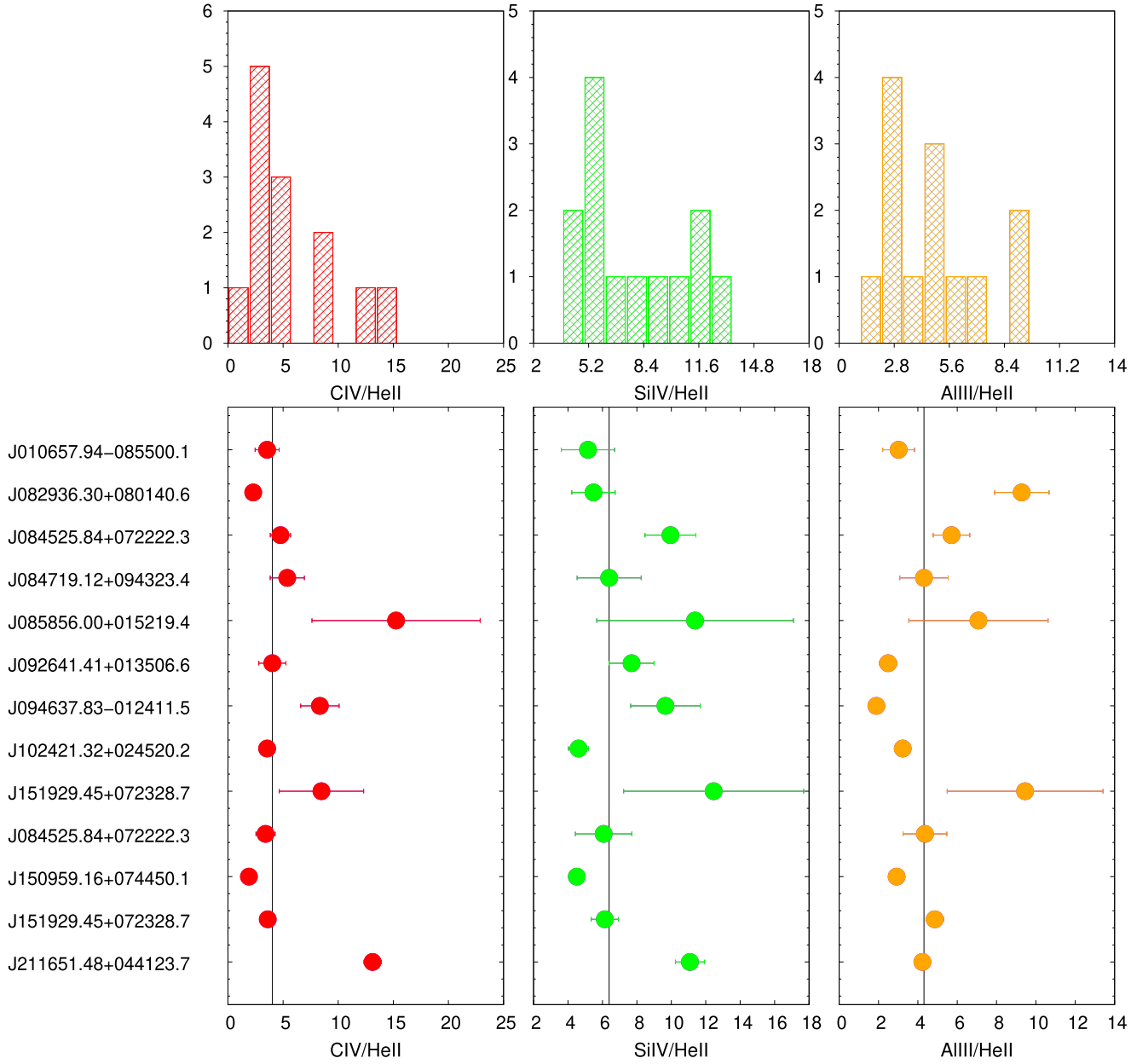

Figure 7. Distribution of diagnostic intensity ratios based on the BC (top) for C IV/He II λ1640 (red), Si IV/He II λ1640 (green), and Al III/He II λ1640 (orange). The bottom panels show results and associated uncertainties for individual sources with the same color-coding as histograms. The vertical black line in the bottom panels represents the median value of sources measurements.

distribution of Z is flat and thin, around $Z \sim 50$–$100\ Z_{\odot}$. This implies that, for a change of the U and $n_{\rm H}$ within the limits allowed by the data, the estimate of Z is stable and independent of U and $n_{\rm H}$. Table 8 reports the individual Z estimates and the SIQR for the sources in the sample (the last row is the median).

The allowed parameter space volume for BLUE is by far less constrained. The right panel of Figure 12 shows the parameter space for the Z estimates from the three BLUE intensity ratios. The condition on the χ^2 distribution is the same as used for the BC, namely, that the data points all satisfy the condition $\chi^2 \leqslant \chi^2_{\rm min} + 1$. A similar shape is obtained if we consider the condition that all three ratios agree with the ones predicted by the model within 1σ. The spread in ionization and density is very large, although the concentration of data points is higher in the case of low $n_{\rm H}$ (log $n_{\rm H} \sim 8$–9 [cm^{-3}]) and high ionization (log $U \sim 0$). At any rate the spread of the data points indicates that solutions at low ionization and high density are also possible. The results for individual sources tend to disfavor this scenario for the wide majority of the objects, but the properties of the gas emitting the BLUE component are less constrained than the ones of the gas emitting the BC. What is missing for BLUE is especially a firm diagnostic of density that in the case of BC is provided mainly by the ratio Al III/He II λ1640. Results on Z are, however, as stable as for the BC, even if the dispersion is larger, and suggest values in the range $10\ Z_{\odot} \lesssim Z \lesssim 50\ Z_{\odot}$.

Summing up, all meaningful estimators converge toward high Z values, definitely supersolar, with $Z \gtrsim 10\ Z_{\odot}$. Ratios C IV/Si IV significantly less than <1 are predicted in the parameter space. Si IV/He II λ1640 seems to give the largest estimates of Z. Also, the high Al III/C IV requires high values of Z. A conclusion has to be tentative, considering the possible

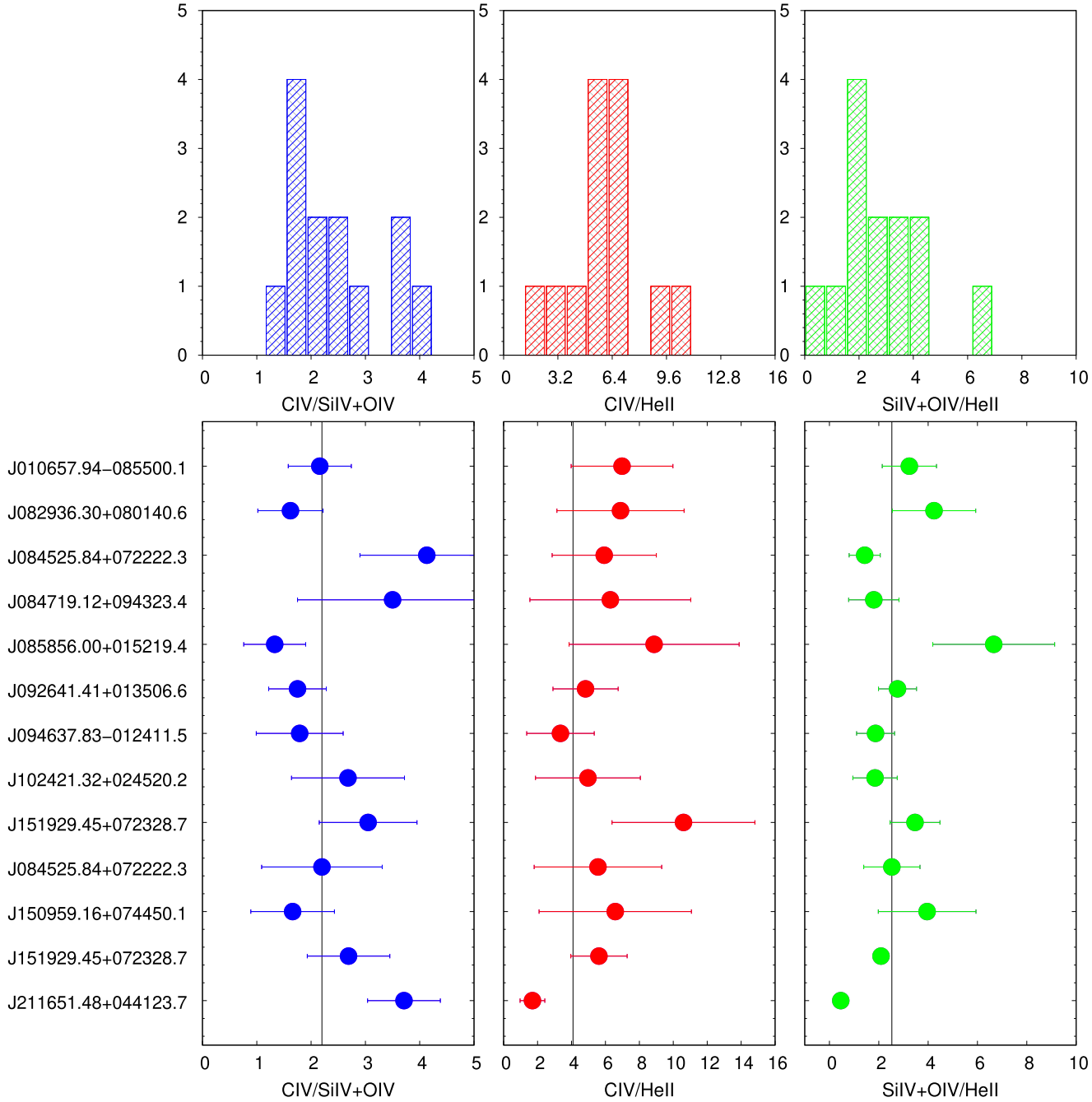

Figure 8. Distribution of diagnostic intensity ratios based on the BLUE components (top) for C IV/[S II] λλ6731, 6717 + O IV] (blue), C IV/He II λ1640 (red), and Si IV + O IV]/He II λ1640 (green). The bottom panels show results and associated uncertainties for individual sources with the same color-coding as histograms, as in the previous figure. The vertical black line represents the median value of ratio measurements.

systematic errors affecting the estimates of the C IV and Si IV intensities: for C IV, the BC in the most extreme cases is often buried under an overwhelming BLUE; a fit is not providing a reliable estimate of the BC (by far the fainter component) but provides a reliable BLUE intensity; for Si IV we may overestimate the intensity due to "cancellation" of the BLUE by absorptions. This said, the present data are consistent with the possibility of a selective enhancement of Al and Si, as already considered by Negrete et al. (2012). This issue will be briefly discussed in Section 5.

At any rate, the absence of correlation between BLUE and BC parameters (Figure 9), the difference in the diagnostic ratios and differences in inferred Z, and the results for individual sources described below justify the approach followed in the paper to maintain a separation between BLUE and BC. The meaning of possible systematic differences between the BC and BLUE is further discussed in Section 5.

4.4.1. Individual Sources

BC.—The best $n_{\rm H}$, U, and Z for each object have been obtained by minimizing the χ^2 as defined in Equation (8), and they are reported in Table 9. The $\chi^2_{\rm min}$ values are listed in the second column of Table 9. At the side of each value there is the uncertainty range for each parameter defined from volume in

Table 6
Metallicity ($\log Z$) of the BC Assuming Fixed U, $n_{\rm H}$

SDSS JCODE	C IV/He II λ1640	Si IV/He II λ1640	Al III/He II λ1640
J010657.94−085500.1	$1.16^{+0.26}_{-0.33}$	$1.85^{+0.20}_{-0.20}$	$1.7^{+0.16}_{-0.15}$
J085856.00+015219.4	$2.22^{+0.36}_{-0.35}$	$2.41^{+0.59}_{-0.36}$	$2.2^{+0.31}_{-0.29}$
J082936.30+080140.6	$0.63^{+0.36}_{-0.65}$	$1.89^{+0.16}_{-0.15}$	$2.36^{+0.10}_{-0.09}$
J084525.84+072222.3	$1.41^{+0.14}_{-0.16}$	$2.31^{+0.11}_{-0.11}$	$2.07^{+0.10}_{-0.09}$
J084719.12+094323.4	$1.50^{+0.20}_{-0.23}$	$1.99^{+0.21}_{-0.19}$	$1.91^{+0.17}_{-0.17}$
J092641.41+013506.6	$1.27^{+0.24}_{-0.29}$	$2.12^{+0.12}_{-0.12}$	$1.59^{+0.11}_{-0.10}$
J094637.83−012411.5	$1.80^{+0.15}_{-0.14}$	$2.29^{+0.16}_{-0.15}$	$1.44^{+0.12}_{-0.13}$
J102421.32+024520.2	$1.16^{+0.11}_{-0.12}$	$1.77^{+0.09}_{-0.08}$	$1.74^{+0.07}_{-0.06}$
J102606.67+011459.0	$1.82^{+0.30}_{-0.32}$	$2.49^{+0.51}_{-0.32}$	$2.38^{+0.27}_{-0.26}$
J114557.84+080029.0	$1.12^{+0.22}_{-0.27}$	$1.96^{+0.19}_{-0.18}$	$1.92^{+0.15}_{-0.15}$
J150959.16+074450.1	$0.19^{+0.49}_{-0.47}$	$1.76^{+0.06}_{-0.07}$	$1.69^{+0.05}_{-0.06}$
J151929.45+072328.7	$1.18^{+0.08}_{-0.09}$	$1.97^{+0.08}_{-0.09}$	$1.98^{+0.05}_{-0.05}$
J211651.48+044123.7	$2.11^{+0.04}_{-0.04}$	$2.39^{+0.06}_{-0.06}$	$1.9^{+0.06}_{-0.06}$
Median	1.27 ± 0.32	1.99 ± 0.21	1.91 ± 0.18

Note. Column (1): SDSS identification. Columns (2), (3), and (4): metallicity values for C IV/He II λ1640, Si IV + O IV]/He II λ1640, and Al III/He II λ1640 with uncertainties.

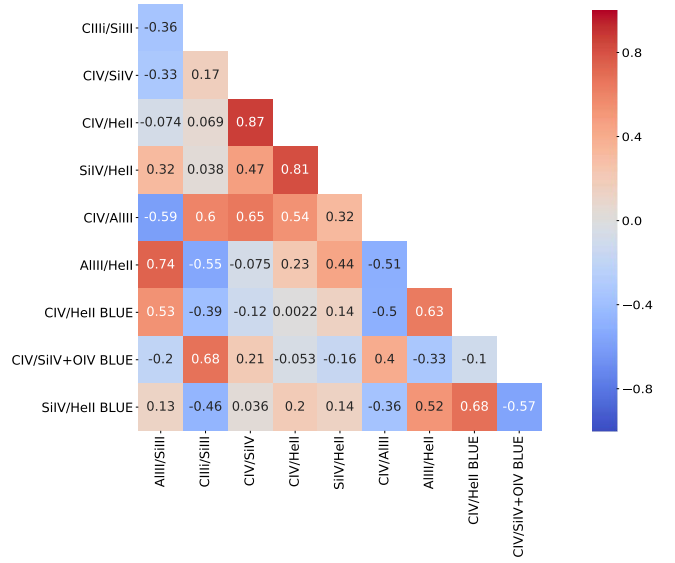

Figure 9. Correlation matrix between diagnostic ratios in BC and BLUE. The numbers in each square show the Spearman rank correlation coefficient. Red colors indicate a positive correlation; blue colors indicate a negative correlation.

the parameter space satisfying the condition $\chi^2 \approx \chi^2_{\rm min} + 1$.[11] In other words, the choice of the best physical conditions was obtained by minimizing the sum of the deviations between the model predictions and the observer diagnostic ratios. The last two rows list the minimum χ^2 values for the median (with the SIQR of the sample from Table 5) and for the median of the values reported for individual sources in Table 9. The obtained values of Z cover the range $5\ Z_\odot \lesssim Z \lesssim 100\ Z_\odot$, with 9 out of 13 sources with $50\ Z_\odot \lesssim Z \lesssim 100\ Z_\odot$, and medians of intensity ratios yielding $Z \sim 50\ Z_\odot$. There is some spread in the ionization parameter values, $-4 \lesssim U \lesssim -1$, but in most cases U indicates low or very low ionization level. The hydrogen density is very high: in only a few cases $\log n_{\rm H} \sim 10$–11, and in several cases $n_{\rm H}$ reaches 10^{14} cm^{-3}. The median values from the ratios are $\log U = -2.25$, $\log n_{\rm H} = 13.75$ (with a range 12.5–14), therefore validating the original assumption of $\log U = -2.5$, $\log n_{\rm H} = 12$ for a fixed physical condition. The results for individual sources confirm the scenario of Figure 12 for the wide majority of the sample sources. The higher $n_{\rm H}$ values are consistent with recent inferences for the low-ionization BLR derived from Temple et al. (2020), based on the Fe III UV emission, which is especially prominent in the UV spectra of xA quasars (Martínez-Aldama et al. 2018a). It is interesting to note that two of the borderline objects (Al III]/Si III] ≈ 0.5, C III]/Si III] ≈ 1) show higher values of the ionization parameter ($\log U \approx -1.0$ to -1.5).

Large ($\gg$1) values of $\chi^2_{\rm min}$ are associated with cases in which the BC components of Al III and/or of Si IV are strong with respect to the BC of C IV, and are further increased by small uncertainty ranges (which are more likely to occur if a line is strong). Intensity ratios C IV/Al III $\lesssim 1$ and C IV/Si IV $\lesssim 1$ are reproduced by photoionization simulations in conditions of very low ionization. The ratio C IV/Al III tends to decrease with increasing Z, although the trend is shallow at the lower ionization levels appropriate for the BC emission (Appendix B). However, high values of the Al III and Si IV + O IV] over He II ratios induced by overabundances could bias the U and lower its values.

BLUE.—The inferences are less clear from BLUE (Table 10, organized like Table 9). In most cases, the permitted volume in the 3D parameter space for individual sources covers a broad range in U and $n_{\rm H}$ as for the median (Figure 12). Figure 12 shows that there is a strip of χ^2 values statistically consistent with the minimum χ^2 that crosses the full domain of the parameter space. Along this strip of permitted values $n_{\rm H}$ and U are linearly dependent, with $\log U \approx -0.5 \cdot n_{\rm H} + 4$ for the median composite ratios. In most sources the U value implies a high degree of ionization, $-1 \lesssim \log U \lesssim 0$, but in three cases (e.g., SDSS J150959.16+074450.1) there is apparently a

[11] This approach follows a standard procedure (Bevington & Robinson 2003, p. 209) for the determination of the confidence intervals, and we see in the matrix $\chi^2(Z, U, n_{\rm H})$ a well-defined global minimum around which the χ^2 increases systematically.

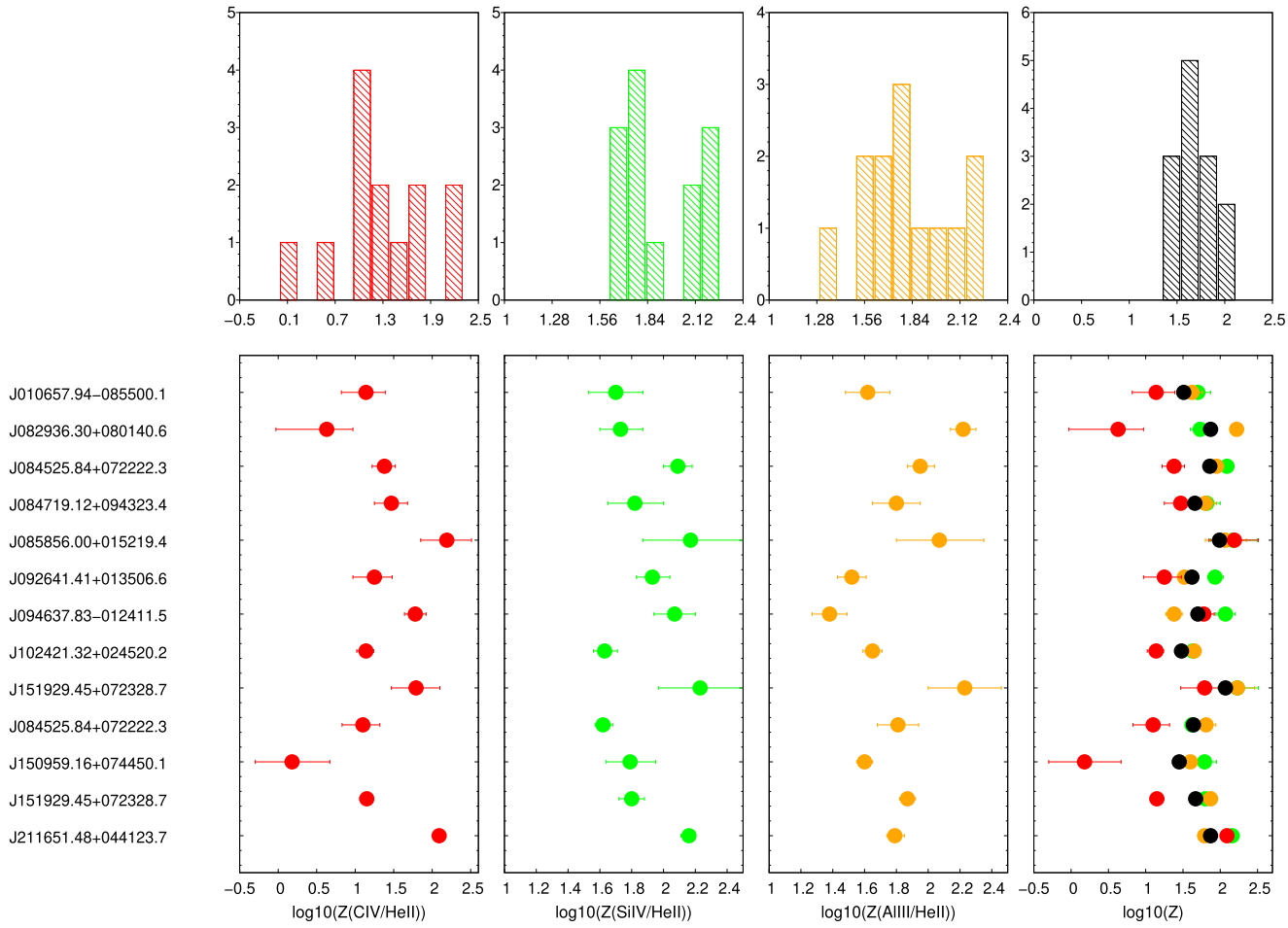

Figure 10. Top panels: distribution of metallicity measurements for the BC obtained from ratios C IV/He II λ1640 (red), Si IV/He II λ1640 (green), and Al III/He II λ1640 (orange), and the mean metallicity obtained from all ratios (black). Bottom panels: results and associated uncertainties for individual sources with the same color-coding as histograms. The last panel contains all metallicity measurements and the mean of them for each object.

Table 7
Metallicity ($\log Z$) of BLUE Assuming Fixed U, $n_{\rm H}$

SDSS JCODE	Si IV + O IV]/He II λ1640	C IV/Si IV + O IV]	C IV/He II λ1640
J010657.94−085500.1	$1.00^{+0.12}_{-0.16}$	$0.88^{+0.14}_{-0.12}$	$1.34^{+0.34}_{-1.99}$
J085856.00+015219.4	$1.26^{+0.20}_{-0.13}$	$1.12^{+0.23}_{-0.21}$	$1.55^{+0.35}_{-2.05}$
J082936.30+080140.6	$1.10^{+0.14}_{-0.16}$	$1.03^{+0.16}_{-0.19}$	$1.33^{+0.41}_{-2.14}$
J084525.84+072222.3	$0.62^{+0.20}_{-0.19}$	$0.63^{+0.09}_{-0.09}$	$1.13^{+0.50}_{-2.07}$
J084719.12+094323.4	$0.72^{+0.27}_{-0.24}$	$0.68^{+0.21}_{-0.15}$	$1.22^{+0.59}_{-2.32}$
J092641.41+013506.6	$0.93^{+0.11}_{-0.14}$	$0.99^{+0.14}_{-0.16}$	$-0.56^{+1.93}_{-0.46}$
J094637.83−012411.5	$0.74^{+0.20}_{-0.18}$	$0.98^{+0.20}_{-0.22}$	$-0.99^{+2.16}_{-1.06}$
J102421.32+024520.2	$0.73^{+0.24}_{-0.20}$	$0.78^{+0.19}_{-0.14}$	$-0.52^{+2.10}_{-0.65}$
J102606.67+011459.0	$1.02^{+0.11}_{-0.12}$	$0.73^{+0.12}_{-0.10}$	$1.67^{+0.24}_{-0.31}$
J114557.84+080029.0	$0.89^{+0.19}_{-0.22}$	$0.87^{+0.25}_{-0.20}$	$0.99^{+0.70}_{-2.12}$
J150959.16+074450.1	$1.07^{+0.18}_{-0.21}$	$1.01^{+0.22}_{-0.23}$	$1.28^{+0.52}_{-2.28}$
J151929.45+072328.7	$0.79^{+0.07}_{-0.06}$	$0.78^{+0.13}_{-0.11}$	$1.02^{+0.40}_{-0.59}$
J211651.48+044123.7	$-0.57^{+0.81}_{-0.43}$	$0.66^{+0.06}_{-0.05}$	$-1.46^{+0.27}_{-0.23}$
Medians	0.89 ± 0.15	0.87 ± 0.13	1.13 ± 0.92

Note. Column (1): SDSS identification. Columns (2), (3), and (4): metallicity values for Si IV + O IV]/He II λ1640, C IV/Si IV + O IV], and C IV/He II λ1640 with uncertainties.

low-ionization solution with U comparable to that of the low-ionization BLR. The medians are $\log n_{\rm H} \sim 7.75$, $\log U \sim -0.5$, close to the values that we assumed for the fixed (U, $n_{\rm H}$) approach. The results on metallicity suggest in most cases $Z \gtrsim 20\ Z_{\odot}$. However, within 1 SIQR from the minimum χ^2, Z values up to 30 are also possible.

Z values from BLUE are systematically lower than those from the BC. The medians differ by a factor of 2. However, a

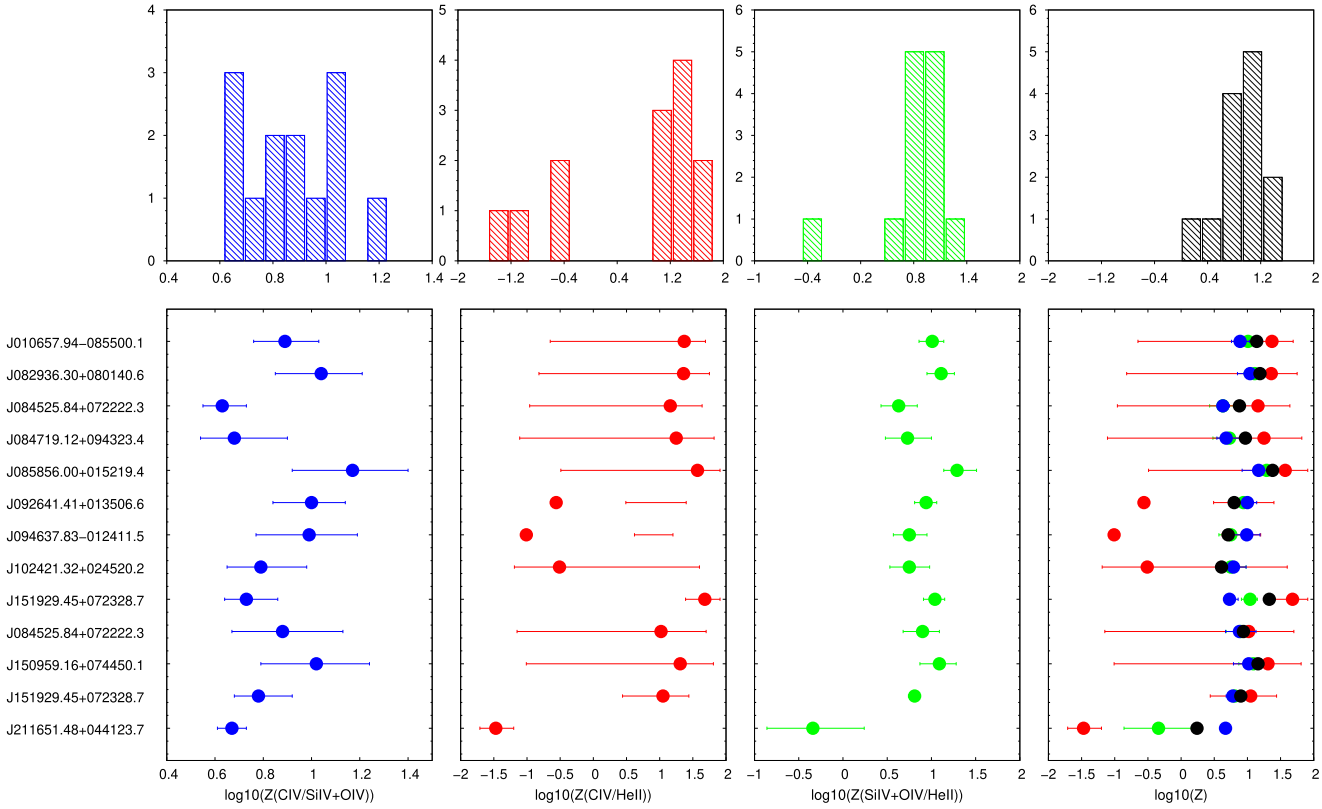

Figure 11. Top panels: distribution of metallicity measurements for blue component obtained from ratios C IV/Si IV + O IV] (blue), C IV/He II λ1640 (red), and Si IV + O IV]/He II λ1640 (green), and the mean metallicity obtained from all ratios (black). Bottom panels: results and associated uncertainties for individual sources with the same color-coding as histograms. The last panel contains all metallicity measurements and the mean of them for each object.

Table 8
Metallicity ($\log Z$) of Individual Quasars Assuming Fixed U, $n_{\rm H}$

SDSS JCODE	~~B~~C	BLUE	Combined
J010657.94−085500.1	1.70 ± 0.34	1.00 ± 0.23	1.34 ± 0.35
J082936.30+080140.6	1.89 ± 0.86	1.10 ± 0.15	1.33 ± 0.43
J084525.84+072222.3	2.07 ± 0.45	0.63 ± 0.25	1.41 ± 0.72
J084719.12+094323.4	1.91 ± 0.25	0.72 ± 0.27	1.50 ± 0.60
J085856.00+015219.4	2.22 ± 0.11	1.26 ± 0.21	2.20 ± 0.48
J092641.41+013506.6	1.59 ± 0.42	0.93 ± 0.77	1.27 ± 0.33
J094637.83−012411.5	1.80 ± 0.42	0.74 ± 0.99	1.44 ± 0.53
J102421.32+024520.2	1.74 ± 0.30	0.73 ± 0.65	1.16 ± 0.51
J102606.67+011459.0	2.38 ± 0.33	1.02 ± 0.47	1.82 ± 0.68
J114557.84+080029.0	1.92 ± 0.42	0.89 ± 0.06	1.12 ± 0.52
J150959.16+074450.1	1.69 ± 0.78	1.07 ± 0.14	1.28 ± 0.34
J151929.45+072328.7	1.97 ± 0.40	0.79 ± 0.12	1.18 ± 0.59
J211651.48+044123.7[a]	2.11 ± 0.24	$0.66 \pm \cdots$	2.11 ± 0.34
Median	1.91 ± 0.16	0.89 ± 0.12	1.34 ± 0.11

Notes. Column (1): SDSS identification. Columns (2), (3), and (4): metallicity medians for BC, BLUE, and a combination of the two, with uncertainties. Column (5): number of ratios used for the BLUE estimates. No uncertainty is reported for BLUE of SDSS J211651.48+044123.7 since only one ratio was used.
[a] Si IV and C IV affected by absorptions on the blue wings.

Welch t-test (Welch 1947) fails to detect a significant difference between the average values of the metallicity for the two components: $t \approx 0.86$ for 5 degrees of freedom (computed using the Welch-Satterthwaite equation) implies a significance of just 80%. Three cases in which the disagreement is large, more than a factor of 5, namely, J084525.84+072222.3, J084719.12+094323.4, and J102606.67+011459.0, are apparently not strongly affected by absorption lines, but the constraints from Tables 10 and 9 are poor, implying that also for BLUE the Z could be much higher. Therefore, we cannot substantiate any claim of a systematic difference between BLUE and BC Z estimates.

The Z, U, $n_{\rm H}$ parameter space occupation of xA quasars.— In summary, the low-ionization BLR of xA sources seems to be consistently characterized by low ionization, extremely high density, and very high metallicity, under the assumption that Z scales with the solar chemical composition. Diagnostics on BLUE is less constraining, and measurements are more difficult. The zero-order results are, however, consistent again with high metallicity $Z \gtrsim 5\ Z_{\odot}$.

The 3D distribution in Figure 12 indicates that, although there might be a large range of uncertainty in the U and $n_{\rm H}$ especially for BLUE, the Z values tend to remain constrained within a narrow strip around a well-defined Z, parallel to the U, $n_{\rm H}$ plane. In other words, Z estimates should be stable, as they are not strongly dependent on the assumed physical parameters.

Comparing the individual Z estimates for fixed and free $n_{\rm H}$ and U (Cols. (2) of Tables 6 and 9) for the BC, the agreement is good, with a median difference of 0.22 and an SIQR of 0.15, with the fixed $n_{\rm H}$ and U being therefore a factor of $\approx$1.65 higher than the one derived assuming a free $n_{\rm H}$ and U. Two sources (J151929.45+072328.7 and J114557.84+080029.0) show a large disagreement, in the sense that the Z values leaving U and $n_{\rm H}$ free are much lower. These Z estimates are, however, highly uncertain, with a shallow χ^2 distribution around the minimum especially for J151929.45+072328.7. For

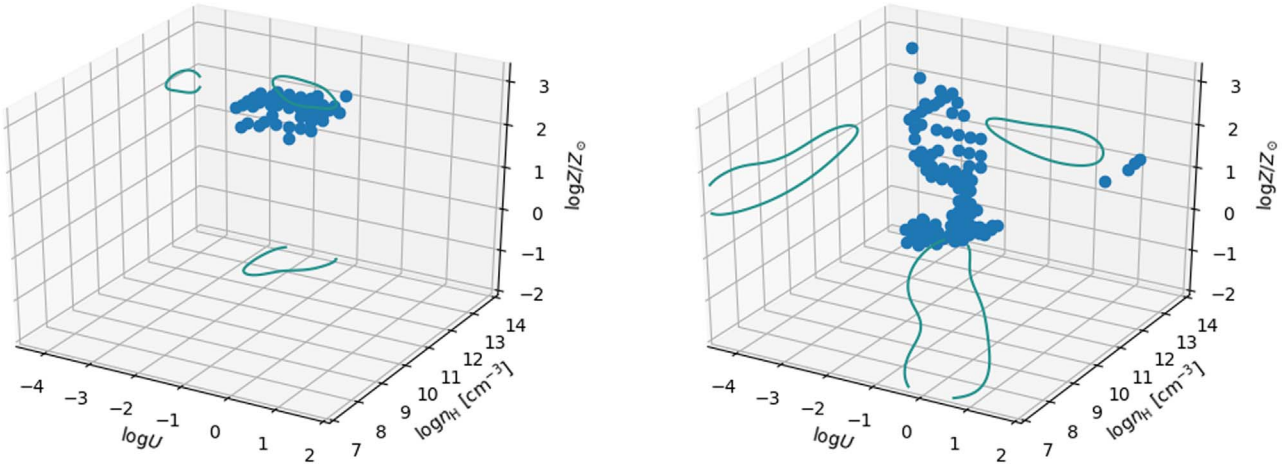

Figure 12. Parameter space $n_{\rm H}$, U, Z. Left: data points in 3D space are elements in the grid of the parameter space selected for not being different from $\chi^2_{\rm min}$ by more than $\delta\chi^2 \approx 1$, computed from the emission-line ratios measured for the BC and referring to the median values in Table 5. Right: same as the left panel, but for the BLUE component, also including the condition that the data points are in agreement with the three diagnostic ratios within the SIQR of the median estimate from Table 5. The individual contour line was smoothed with a Gaussian kernel.

Table 9
Z, U, $n_{\rm H}$ of Individual Sources and Median Derived from the BC

SDSS JCODE (1)	$\chi^2_{\rm min}$ (2)	$\log Z$ ($Z_\odot$) (3)	$\delta \log Z$ ($Z_\odot$) (4)	$\log U$ (5)	$\delta \log U$ (6)	$\log\ n_{\rm H}$ (7)	$\delta \log\ n_{\rm H}$
J010657.94−085500.1	2.6894	1.7	0.7–1.7	−2.00	−2.75 to −1.25	13.50	12.00–14.00
J082936.30+080140.6	6.6414	1.3	0.7–2.7	−4.00	−4.00 to −3.50	14.00	12.75–14.00
J084525.84+072222.3	13.700	1.7	1.0–3.0	−1.75	−3.75 to −0.25	14.00	12.00–14.00
J084719.12+094323.4	1.7004	1.7	1.0–2.0	−2.25	−2.50 to −1.50	13.75	12.50–14.00
J085856.00+015219.4	0.0012	2.0	1.7–2.7	−2.25	−3.00 to −1.75	12.50	12.00–14.00
J092641.41+013506.6	1.7982	1.7	1.7–2.0	−1.50	−1.75 to −1.00	14.00	13.50–14.00
J094637.83−012411.5	0.3253	1.7	1.7–2.3	−1.00	−1.25 to −0.75	12.25	11.75–14.00
J102421.32+024520.2	15.819	1.7	1.3–2.0	−2.25	−3.00 to −1.50	13.50	12.75–14.00
J102606.67+011459.0	1.5020	2.0	1.7–2.3	−1.75	−2.50 to −0.75	14.00	12.50–14.00
J114557.84+080029.0	6.6174	0.7	0.7–2.0	−3.75	−3.75 to −1.25	14.00	12.25–14.00
J150959.16+074450.1	45.287	1.3	0.5–2.0	−1.75	−0.50 to −3.50	13.75	12.25–14.00
J151929.45+072328.7	29.220	0.7	0.3–3.0	−3.75	−4.00 to −2.75	14.00	11.00–14.00
J211651.48+044123.7	1.4476	2.0	1.7–2.0	−2.00	−2.00 to −0.75	12.25	10.75–12.25
$\mu_{\frac{1}{2}}$(Ratios)	1.9914	1.7	0.7–2.0	−2.25	−2.75 to −1.25	13.75	12.50–14.00
$\mu_{\frac{1}{2}}$(Objects)	⋯	1.7	1.5–1.9	−2.00	−2.25 to −1.75	13.75	13.50–14.00

Table 10
Z, U, $n_{\rm H}$ of Individual Sources and Median Derived from BLUE

SDSS JCODE (1)	$\chi^2_{\rm min}$ (2)	$\log Z$ ($Z_\odot$) (3)	$\delta \log Z$ ($Z_\odot$) (4)	$\log U$ (5)	$\delta \log U$ (6)	$\log\ n_{\rm H}$ (7)	$\delta \log\ n_{\rm H}$
J010657.94−085500.1	0.00985	1.70	0.70–1.7	0.75	−1.5–0.75	7.75	7.50–9.75
J082936.30+080140.6	0.01506	1.30	1.00–1.70	−0.25	−2.0 to −0.00	8.00	7.75–12.25
J084525.84+072222.3	0.00143	1.0	0.00–2.30	−1.50	−2.50 to −1.25	7.25	7.00–11.25
J084719.12+094323.4	0.00097	1.00	0.00–3.00	−2.24	−2.50–0.75	8.75	7.50–11.50
J085856.00+015219.4	0.00305	1.70	1.0–2.00	0.50	−1.75–0.50	8.25	7.00–11.75
J102606.67+011459.0	0.00111	0.70	0.70–3.00	−1.00	−2.50 to −0.5	9.25	8.25–11.25
J114557.84+080029.0	0.00164	1.30	0.30–1.70	−2.50	−2.50–0.25	11.50	7.25–12.50
J150959.16+074450.1	0.00288	1.30	0.30–2.00	−2.00	−2.75–0.75	11.75	7.00–13.75
J151929.45+072328.7	0.00032	0.30	0.30–1.30	−0.50	−0.75–0.25	10.00	7.75–10.25
$\mu_{\frac{1}{2}}$(Ratios)	0.07336	1.30	1.0–1.30	−0.50	−0.50 to −0.50	7.75	7.75–8.00
$\mu_{\frac{1}{2}}$(Objects)	⋯	1.30	1.15–1.45	−1.00	−0.125 to −1.875	8.75	7.75–9.75

this object the maximum metallicity covered by the simulations $Z = 1000\ Z_{\odot}$ is still consistent within the uncertainties.

5. Discussion

5.1. A Method to Estimate Z

The determination of the metal content of the broad-line-emitting region of xA quasars was made possible by the following procedure:

1. The estimation of an accurate redshift. Even if all lines are affected by significant blueshifts that reduce the values of measured redshift, in the absence of information from the Hβ spectral range the Al III and the λ1900 blend can be used as proxies of proper redshift estimators. The blueshifts are the smallest in the intermediate-ionization lines at λ1900 (A. del Olmo et al. 2021, in preparation).
2. The separation of the BC and BLUE, for C IV and the λ1400 blend. The line width of the individual components of the Al III doublet can be used as a template BC. The component BLUE is defined as the excess emission on the blue side of the BC.
3. A first estimate of metallicity can be obtained from the assumption that the low-ionization BLR associated with the BC and wind/outflow component associated with BLUE can be described by similar physical conditions in different objects. Several diagnostic ratios can be associated with the intensity ratios predicted by an array of photoionization simulations, namely,
   (a) for the BC: Al III/He II λ1640, C IV/He II λ1640, Si IV/He II λ1640, assuming $(\log U, \log n_{\rm H}) = (-2.5, 12)$ or $(\log U, \log n_{\rm H}) = (-2.5, 13)$;
   (b) for the BLUE: C IV/He II λ1640, Si IV + O IV]/He II λ1640, C IV/Si IV + O IV] assuming $(\log U, \log n_{\rm H}) = (0, 9)$.
4. Estimates can be refined for individual sources relaxing the constant $(\log U, \log n_{\rm H})$ assumptions. Tight constraints can be obtained for the BC. The BLUE is more problematic, because of both observational difficulties and the absence of unambiguous diagnostics.

Our method relies on ratios involving He II λ1640 that have not been much considered in previous literature. In addition, we have considered fixed SED, turbulence (equal to 0), and column density in the simulations ($N_{\rm c} = 10^{23}$) as fixed. The role of turbulence is further discussed in Section 5.5 and is found to be not relevant, unlike in the case of Fe II emission in the optical spectral range, where effects of self- and Lyα-fluorescence are important (e.g., Verner et al. 1999; Panda et al. 2018), while the $N_{\rm c}$ effect is most likely negligible.

Extension of the method to the full Population A is a likely possibility, since we do not expect a very strong effect of the SED on the metallicity estimate, as long as the SED has a prominent big blue bump, as seems to be case for Population A. The role of SED is likely important if the method has to be extended to sources of Population B along the main sequence. At least two SED cases should be considered, if the aim is to apply the method presented in this paper to a large sample of quasars.

Intensity ratios involving He II λ1640 are difficult to measure in the xA spectra but may be more accessible for Population B spectra. Ferland et al. (2020) have shown significant differences in the SED as a function of $L/L_{\rm Edd}$, with a much flatter SED at low $L/L_{\rm Edd}$. The extension to Population B would therefore require a new dedicated array of simulations.

5.2. Accretion Parameters of Sample Sources

The bolometric luminosity has been computed assuming a flat ΛCDM cosmological model with $\Omega_{\Lambda} = 0.7$, $\Omega_m = 0.3$, and $H_0 = 70\ {\rm km\ s^{-1}\ Mpc^{-1}}$. Following Marziani & Sulentic (2014), we decided to use Al III as a virial broadening estimator for computing the $M_{\rm BH}$. Our estimates adopt two different scaling laws: the scaling laws of Vestergaard & Peterson (2006) for C IV, and a second, unpublished one based on Al III (A. del Olmo et al. 2021, in preparation). Eddington ratios have been obtained using the Eddington luminosity $L_{\rm Edd} \approx 1.3 \times 10^{38} (M_{\rm BH}/M_{\odot})\ {\rm erg\ s^{-1}}$. The luminosity range of the sample is very limited, less than a factor of 3, $46.8 \lesssim \log L \lesssim 47.3$, in line with the requirement of similar redshift and high flux values. Correspondingly, the $M_{\rm BH}$ and the Eddington ratio are constrained in the range $8.8 \lesssim \log M_{\rm BH} \lesssim 9.5$ and $-0.55 \lesssim \log L/L_{\rm Edd} \lesssim 0.18$, respectively. The $M_{\rm BH}$ sample dispersion is small, with $\log M_{\rm BH} \sim 9.4 \pm 0.2\ [M_{\odot}]$. The scatter in $M_{\rm BH}$ and $L/L_{\rm Edd}$ is reduced to $\approx$0.1 dex if we exclude one object with the lowest $M_{\rm BH}$ and highest $L/L_{\rm Edd}$. Applying a small correction (10%) to the FWHM to account for an excess broadening in Al III due to nonvirial motions will decrease the $M_{\rm BH}$ by 0.1 dex (as found by Negrete et al. 2018 for Hβ) and increase $L/L_{\rm Edd}$ correspondingly. If this correction is applied, the median $L/L_{\rm Edd}$ is $\approx$0.6. Using the C IV BC FWHM as a virial broadening estimator further decreases the $M_{\rm BH}$ median estimate by 0.1 dex. The accretion parameters are consistent with extreme quasars of Population A at high mass and luminosity; they are mainly at the low-$L/L_{\rm Edd}$ end of sample 3 (based on $M_{\rm BH}$ estimates from Al III) of Marziani & Sulentic (2014). The small dispersion in physical properties of the present sample (0.2 dex) focuses the analysis on properties that may differ for fixed accretion parameters, and fixed ratio of radiation and gravitation forces, perhaps related to different enrichment histories.

5.2.1. Correlation between Diagnostic Ratios and AGN Physical Properties

Considering the small dispersion in $M_{\rm BH}$, $L/L_{\rm Edd}$, and bolometric luminosity, it is hardly surprising that none of the ratios utilized in this paper are significantly correlated with the accretion parameter. The highest degree of correlation is seen between $L/L_{\rm Edd}$ and C IV/Al III, but still below the minimum ρ needed for a statistically significant correlation.

In Figure 13 we present the correlation between metallicity and diagnostic ratios, along with log of bolometric luminosity, log of black hole mass, and log of Eddington ratio, for BC and BLUE. The strongest correlations between $Z_{\rm BC}$ and intensity ratios are with Si IV/He II λ1640 (0.75) and Al III/He II λ1640 (0.77). For $Z_{\rm BLUE}$, Si IV/He II λ1640 (BLUE components) correlates strongly (0.99). $Z_{\rm BLUE}$ correlates with physical parameters, whereas $Z_{\rm BC}$ rather anticorrelates with them, but not at a statistically significant level. Considering the limited range in luminosity and $M_{\rm BH}$ and the small sample size, these trends should be confirmed.

The metallicity values we derive are very high among quasars analyzed with similar techniques (e.g., Nagao et al. 2006b; Shin et al. 2013; Sulentic et al. 2014): as mentioned, typical values for high-z quasars are around 5 $Z_{\odot}$. This value

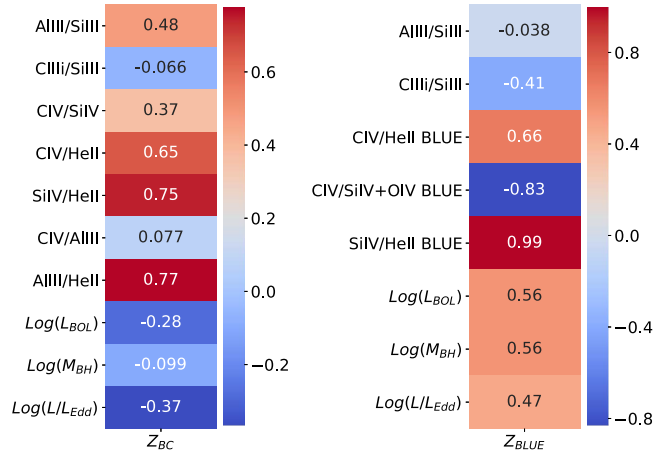

Figure 13. Left panel: correlation matrix between Z computed for the BC and BC diagnostic ratios assuming fixed $n_{\rm H}$ and U along with log of bolometric luminosity, log of black hole mass, and log of Eddington ratio. Right panel: same as the left panel, but for the BLUE component. The numbers in each square show the Spearman rank correlation coefficient. The color hue is proportional to the correlation, from dark blue (strong negative correlation) to red (strong positive correlation).

could be taken as a reference over a broad range of redshift, and also for the sample considered in the present paper, as there is no evidence of metallicity evolution in the BLR up to $z \approx 7.5$ (e.g., Nagao et al. 2006b; Juarez et al. 2009; Xu et al. 2012; Onoue et al. 2020). This is in line with the results of Negrete et al. (2012), who found very similar intensity ratios for the prototypical NLSy1 and xA source I Zw 1, of relatively low luminosity at low z, and a luminous xA object at redshift $z \approx 3.23$. Even if these authors did not derive Z from their data, the I Zw 1 intensity ratios reported in their paper indicate very high metallicity, consistent with the values derived for the present sample.

More than inferences on the global enhancement of Z in the host galaxies, the absence of evolution points toward a circumnuclear source of metal enrichment, ultimately associated with a starburst (e.g., Collin & Zahn 1999a; Xu et al. 2012).

A detailed comparison with previous work on the dependence of Z on accretion parameters is hampered by two difficulties: (1) Before comparing the intensity ratios of this paper, we should consider that other authors do not distinguish between BLUE and BC when computing the ratios. This has the unfortunate implication that in some cases, such as Al III/C IV, the ratio is taken between lines emitted predominantly in different regions (virialized and wind), presumably in very different physical conditions. Not distinguishing between BC and BLUE yields C IV/Al III $\sim 10 \gg 1$. (2) Methods of $M_{\rm BH}$ estimate differ. For example, Matsuoka et al. (2011) use the Vestergaard & Peterson (2006) scaling laws without any correction to the line width of C IV. This might easily imply overestimates of the $M_{\rm BH}$ by factors of 5–10 (Sulentic et al. 2007). The analysis by Shemmer et al. (2004) instead used Hβ from optical and IR observations to compute $M_{\rm BH}$ and to examine the dependence of metallicity on accretion parameters. These authors found the strongest dependence on Eddington ratio (with respect to luminosity and mass) over 6 orders of magnitude in luminosity, suggesting that luminosity and black hole mass are less relevant (as also found, e.g., by Shin et al. 2013).

5.3. A Posteriori Analysis of N V Strength

As was stressed in several works (e.g., Wang et al. 2012a; Sulentic et al. 2014), the intensity of the N V line is difficult to estimate owing to blending with Lyα and strongly affected by absorption. We model Lyα and N V using the same criteria as in Si IV modeling. However, in this work, we give only a qualitative judgment of N V strength for our sample, because of large uncertainties due to the effect mentioned above. For sources in the highest metallicity range obtained from ratios from BC, the N V BC intensity is slightly higher than or comparable to Lyα BC. Blue components dominate both lines. We notice also significantly higher intensity of the blue component in comparison to the broad one in Si IV and C IV blends. An example of source of this type is shown in the upper half of Figure 14. On the contrary, sources with the lowest metallicities obtained from BC intensity ratios show the Lyα BC intensity higher than in N V, and the BC is stronger than BLUE. We see the same behavior of strong BC in the Si IV and C IV ranges. An example of sources of this type is shown in the lower half of Figure 14. Shin et al. (2013) compared Si IV + O IV] and N V fluxes and found strong, significant correlation between them ($\rho = 0.75$). The N V over He II λ1640 or Hβ should be a strong tracer of Z, as it is sensitive to secondary Z production and hence proportional to Z^2 (Hamann & Ferland 1999). Therefore, we conclude that the N V emission is extremely strong and consistent with very high metal content. A much more thorough investigation of the quasar absorption/emission system is needed to include N V as a Z estimator. This is deferred to further work.

5.4. Role of Column Density

The column density assumed in the present paper is log $N_{\rm c} = 23$ [cm^{-2}]. With this value the emitting clouds in the low-ionization conditions remain optically thick to the Lyman continuum for most of the geometrical depth of the cloud. Even if the value log$N_{\rm c} = 23$ may appear as a lower limit for the low-ionization BLR, as higher values are required to explain low-ionization emission such as Ca II and Fe II (Panda 2020; Panda et al. 2020a), the emission of the intermediate- and high-ionized region is confined within the fully ionized part of the line-emitting gas, whose extension is already much less than the geometrical depth of the gas slab for log$N_{\rm c} = 23$. Therefore, we expect no or a negligible effect from an increase in the column density for the low-ionization part of the BLR.

For BLUE, the situation is radically different, and we have no actual strong constraints on column density. Most emission may come from a clumpy outflow (Matthews 2016 and references therein), and therefore assuming a constant $N_{\rm c}$ may not be appropriate. Considering the poor constraint that we are able to obtain, we leave the issue to an eventual investigation.

5.5. Role of Turbulence

The results presented in this work refer to the case in which there is no significant microturbulence included in the CLOUDY computations. Figure 15 shows that at low ionization the effect is relatively modest, and that in the high-ionization case appropriate for BLUE the effect is very modest. Less obvious is the behavior at low ionization for $R_{\rm Fe\,II}$: it shows an increase for $t = 10$ km s^{-1}, but then it has a surprising drop at a larger value of the microturbulence. While the increase can be explained by an increase of the transitions for which fluorescence is possible,

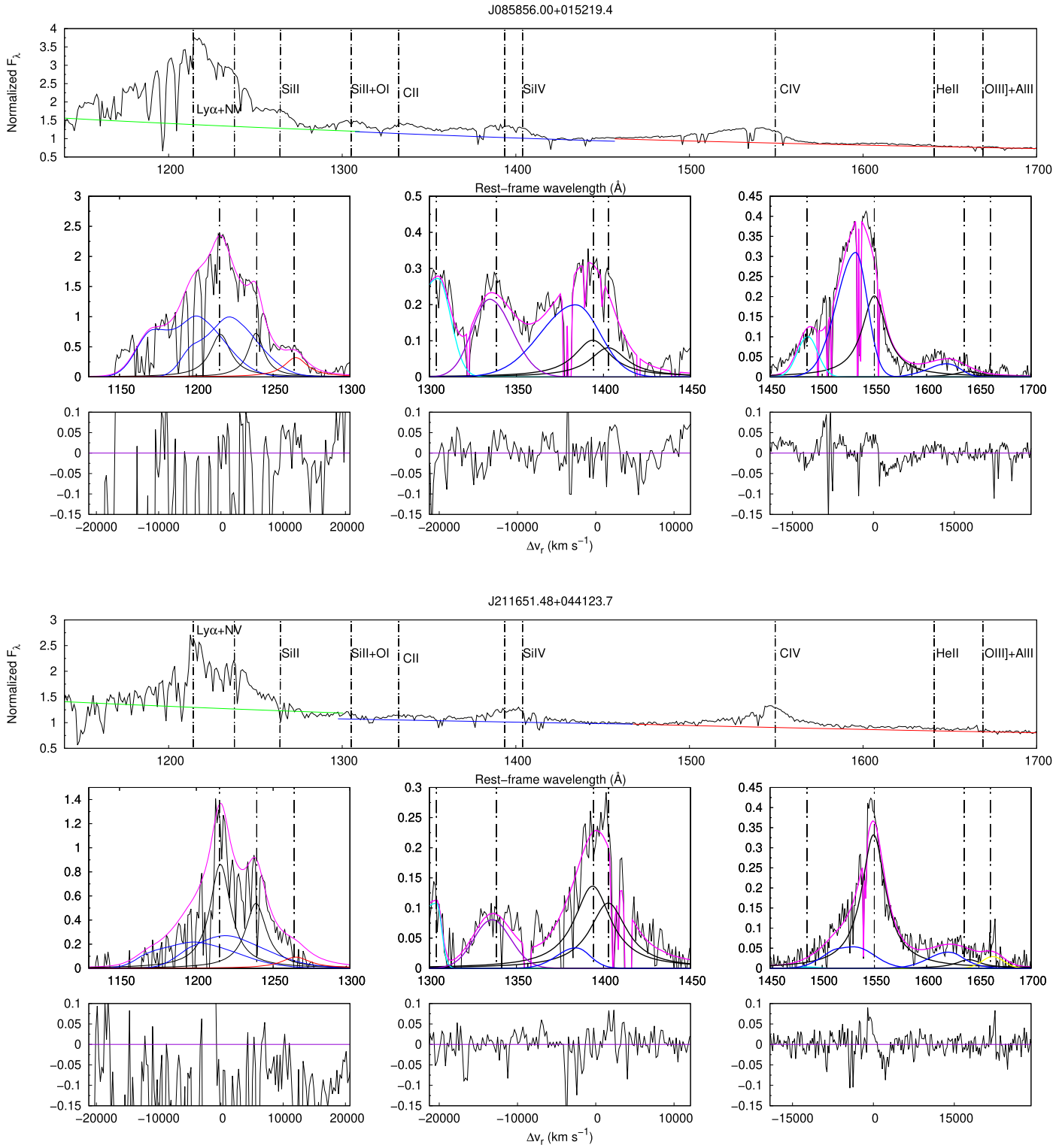

Figure 14. Analysis of sources showing the Lyα + N V blend. Top: calibrated rest-frame spectrum of SDSS J085856.00+015219.4, before continuum subtraction. Global or local continuum is specified by a solid colored line, while the black line marks rest-framed data. Dotted–dashed vertical lines correspond to the rest-frame wavelength of each emission line. Bottom: multicomponent fits after continuum subtraction for the Lα λ1216, Si IV λ1397, and C IV λ1549 spectral ranges. The solid black line marks the BC at rest frame associated with Lyα λ 1216, N V λ1240, Si IV λ1397, and C IV λ1549. The blue one marks the blueshifted component associated with each emission. The magenta line corresponds to the fit to the whole spectrum. In the bottom left panel, the red line corresponds to Si II λ1265. In the middle bottom panel, the light-blue line marks the contribution of the O I + Si II λ1304 blend, while the violet line corresponds to the C II λ1335 emission line. In the C IV λ1549 region, N IV] λ1486 is represented by a light-blue line, while the gold one corresponds to the O III] λ1663 + Al II λ1670 blend. Lower panels correspond to the residuals, in radial velocity units km s^{-1} and in Å. Bottom: same as in the previous panels, but for SDSS J211651.48+044123.7.

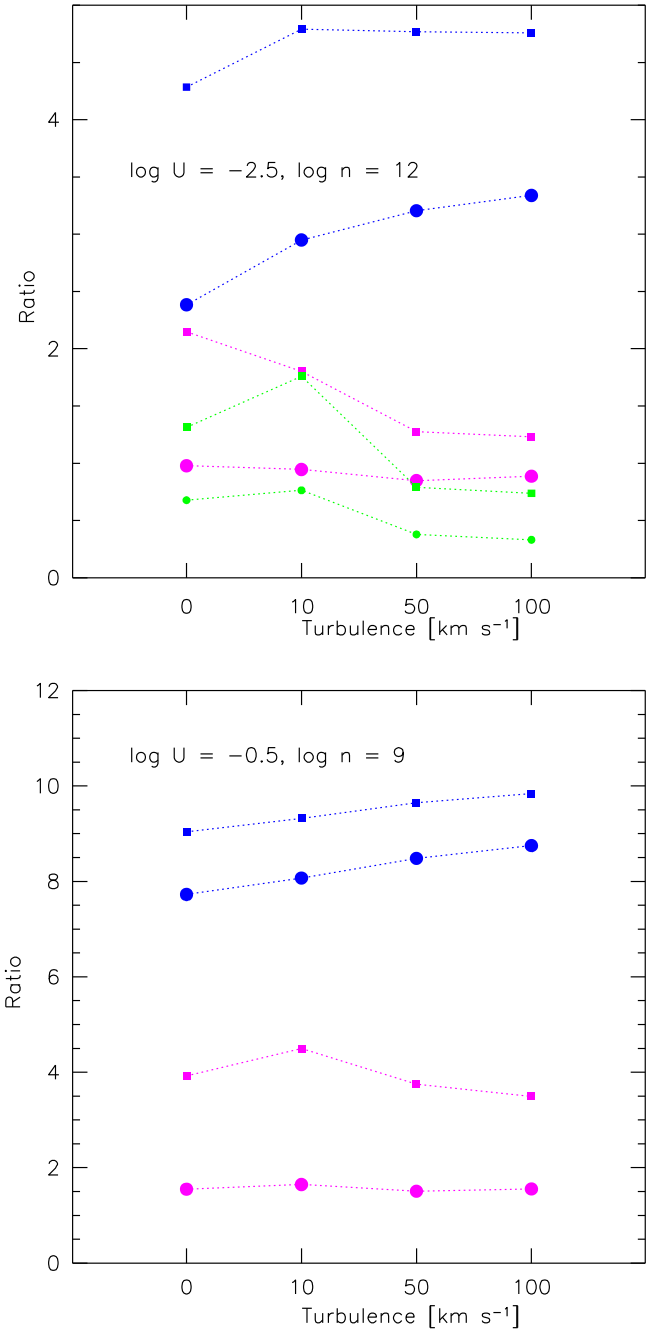

Figure 15. Effects of turbulence on diagnostic line ratios, for C IV/He II λ1640 (blue) and Si IV/He II λ1640 (magenta), considering 5 (circles) and 20 $Z_{\odot}$ (squares), according to CLOUDY 13.05 computations. The top panel assumes the low-ionization conditions appropriate for BC emission, the bottom one for BLUE. In the top panel the green lines trace the same trends for the Fe II blend at λ4570 over Hβ ratio, i.e., $R_{\rm Fe\ II}$.

the decrease is not of obvious interpretation. It has been, however, confirmed by the independent set of simulations of Panda et al. (2018, 2019).

5.6. Metal Segregation?

Metals are expected to be preferentially accelerated by resonance scattering (e.g., Proga 2007b; Risaliti & Elvis 2010). In principle, for a sufficiently large photon flux, the acceleration of metals by radiation pressure might become larger than the Coulomb friction, therefore causing a decoupling of the metals with respect to their parent plasma (Baskin & Laor 2012). This possibility has been explored in the context of the BALs, and broad absorption and emission components are expected to be related (Elvis 2000; Xu et al. 2020). The ionization parameter values are, however, several orders of magnitudes higher than the ones derived for the BLUE emission component. In addition, our Z estimates for the BLUE suggest, if anything, values lower than or equal to those for the BC, whose Z might be related more to the original chemical composition of the gas in the accretion material. However, we ascribe the systematic differences between BC and BLUE as uncertainties in the method and measurement, so that Z from BLUE and BC should be considered intrinsically equal.

Considering that the most metal-rich stars, galaxies, and molecular clouds in the universe do not exceed $Z \approx 5\ Z_{\odot}$ (Maiolino & Mannucci 2019), circumnuclear star formation is needed for the chemical enrichment of the BLR gas (e.g., Collin & Zahn 1999a, 1999b; Wang et al. 2011, 2012b). Star formation may occur in the self-gravitating, outer part of the disk. An alternative possibility is that a massive star could be formed inside the disk by accretion of disk gas (Cantiello et al. 2020).

5.7. Abundance Pollution?

An implication of the scenarios involving circumnuclear or even nuclear star formation is that there could be an alteration of the relative abundance of elements with respect to the standard solar composition (Anders & Grevesse 1989; Grevesse & Sauval 1998). Support for this hypothesis is provided by the extreme C IV/Si IV and C IV/Al III that may hint at a selective enhancement of Al with respect to C. As suggested by Negrete et al. (2012), core-collapse supernovæ with very massive progenitors could be at the origin of a selective enhancement. Supernovae with progenitors of masses between 15 and 40 $M_{\odot}$ have selective enhancement in their yields of Al and Si by factors of $\approx$100 and 10 relative to hydrogen with respect to solar (Chieffi & Limongi 2013). Since carbon is also increased by a factor of $\sim$10 with respect to solar, the [Al/C] is expected to be a factor of $\sim$10 larger than the solar value in supernova ejecta. The case for silicon is less clear, as the enhancement is of the same order of magnitude as the one expected for carbon. Pollution of gas by supernovæ may therefore lead to an estimate of the Z higher than the actual one, if solar relative abundances are assumed. This possibility will be explored in an eventual work (K. Garnica et al. 2021, in preparation).

5.8. Implications for Quasar Structure Evolution

Metallicity and the outflow prominence of quasars were found to be highly correlated (Wang et al. 2012a; Shin et al. 2017). The implication of these results is that xA sources, which show the highest blueshifts (Sulentic et al. 2017; Martinez-Aldama et al. 2018a, 2018b; Vietri et al. 2018), should also be the most metal-rich. The xA sources should be at the top of the Z outflow parameter correlation of Wang et al. (2012a), if $Z \gtrsim 10\ Z_{\odot}$.

There is evidence of a metallicity correlation between the BLR and NLR (Du et al. 2014), as expected if the outflows on spatial scales of kiloparsecs are originating in a disk wind. Zamanov et al. (2002) derived very small spatial scales at low

luminosity. This provides additional support to the idea that xA sources, which at low z phenomenologically appear as Fe II-strong NLSy1s, are relatively young sources. Their low [O III] λ5007 equivalent width implied young age more than orientation effects (Risaliti et al. 2011; Bisogni et al. 2017). The $z \approx 2$ quasars of the present sample are radiating at relatively high $L/L_{\rm Edd}$, although there are no examples of the extremes of xA sources showing blueshifted emission in Al III as prominent as the one of C IV (e.g., Martínez-Aldama et al. 2017). There is no evidence of heavy obscuration. They are certainly out of the obscured early evolution stage in which the accreting black hole is enveloped by gas and dust (see the sketch in D'Onofrio & Marziani 2018). The W C IV distribution covers the upper half of the one of Martínez-Aldama et al. (2018a). There are no weak-lined quasars following Diamond-Stanic et al. (2009). The xA sources of the present sample may have reached a sort of stable equilibrium between gravitation and radiation forces made perhaps possible by the development by an optically thick, geometrically thick accretion disk, and by its anisotropic radiation properties (e.g., Abramowicz et al. 1988; Szuszkiewicz et al. 1996; Sądowski et al. 2014).

The median value of the peak displacement of the BLUE component is $\approx$3500 km s^{-1}, and the centroid at half-maximum is shifted by 5000 km s^{-1}. The extreme blueshifts in the metal lines imply outflows that may not remain bound to the potential well of the black hole and of the inner bulge of the host galaxies (e.g., Marziani et al. 2016b and references therein). The high metal content of the outflows, estimated by the present work to be in the range of 10–50 $Z_{\odot}$, implies that these sources are likely to be a major source of metal enrichment of the interstellar gas of the host galaxy and of the intergalactic medium. Using a standard estimate for the mass outflow rate $\dot{M}$ (Marziani et al. 2016b), $\dot{M} \approx 15 L_{\rm C\,IV,45} v_{5000} r_{\rm 1\,pc}^{-1} n_9^{-1}\, M_{\odot}\, {\rm yr}^{-1}$, we obtain an outflow rate of $\dot{M} \approx 20\, M_{\odot}\, {\rm yr}^{-1}$, assuming median values for the sources of our sample: median outflow velocity from the peak of BLUE ≈ -3500 km s^{-1}, a median luminosity of the C IV BLUE (corrected because of Galactic extinction) of 4.2×10^{44} erg s^{-1}, a median radius 5.9×10^{17} cm from the Kaspi et al. (2007) radius−luminosity correlation for C IV, and $n_9 = 1$. For a duty cycle of $\sim 10^8$ yr, the expelled mass of heavily enriched gas could be $\sim 10^9\, M_{\odot}$.

6. Conclusion

The sources at the extreme end of Population A along the main sequence are defined by the prominence of their Fe II emission and, precisely, by the selection criterion $R_{\rm Fe\,II} \gtrsim 1$ (Marziani & Sulentic 2014; Du et al. 2016a). Their properties as a class are scarcely known. Even if there has been a long history of studies focused on Fe II-strong sources since Lipari et al. (1993) and Graham et al. (1996), their relevance to galactic and large-scale structure evolution is being reconsidered anew with the help of the quasar main sequence. This paper adds to other aspects that were considered by previous investigations (e.g., the very powerful outflows, the disjoint low- and high-ionization emitting regions, first suggested by Collin-Souffrin et al. 1988), a quantitative analysis of the chemical composition of xA sources. The main aspects of the present investigations can be summarized as follows:

1. We distinguish between two emission-line components most likely originating from emitting in widely different physical conditions: a virialized low-ionization BLR, and a high-ionization region associated with a very strong blueshifted excess in the C IV emission line. This is the conditio sine qua non for meaningful Z estimates.
2. The physical conditions in the low and high regions were confirmed to be very different, with the low ionization (U, $n_{\rm H}$) $\approx$ (−2.75, 12.5–14) and the high ionization (U, $n_{\rm H}$) $\approx$ (−0.5, 8). The high-ionization region parameters are, however, poorly constrained.
3. Using intensity ratios between the strongest metal lines and He II λ1640 emission at λ1640, we derive metallicity values in the range $10\, Z_{\odot} \lesssim Z \lesssim 50\, Z_{\odot}$, with most likely values around several tens of the solar metallicity. Incidentally, we note that the low equivalent width is consistent with the high Z of the emitting regions.
4. We find evidence of overabundance of Al with respect to C. This result points toward possible pollution of the broad-line-emitting gas chemical composition by supernova ejecta.

xA quasars are perhaps the only quasars whose ejection are able to overcome the potential well of the black hole and of the host galaxy. Applying the method to large samples of quasars would permit us to constrain the metal enrichment processes on a galactic scale.

The present analysis relied heavily on the He II λ1640 line, which is of low equivalent width and with a flat, very broad profile. Therefore, a more precise analysis would require spectra of moderate dispersion but of higher S/N. A large part of the scatter and/or systematic difference for various Z estimators is related to the difficulty in isolating faint and broad emission in relatively noisy spectra.

M.S. acknowledges the support of the Erasmus+ program of the European Union and would like to express very great appreciation to Istituto Nazionale di Astrofisica (INAF) Osservatorio Astronomico di Padova, University of Padova, and Astronomical Observatory of the University of Warsaw for enabling her to complete an internship. The project was partially supported by the Polish Funding Agency National Science Centre project 2017/26/A/ST9/00756 (MAESTRO 9) and MNiSW grant DIR/WK/2018/12. P.M. acknowledges the Hypatia of Alexandria visiting grant SO-IAA (SEV-2017-0709) through the Center of Excellence Severo Ochoa and is deeply indebted to Drs. J. Perea and A. del Olmo for the generous allocation of computing resources and for a stay at IAA. A.d.O. acknowledges financial support from the Spanish grants MCI PID2019-106027GB-C41 and the State Agency for Research of the Spanish MCIU through the "Center of Excellence Severo Ochoa" award for the Instituto de Astrofísica de Andalucía (SEV-2017-0709).

Funding for the Sloan Digital Sky Survey (SDSS) has been provided by the Alfred P. Sloan Foundation, the Participating Institutions, the National Aeronautics and Space Administration, the National Science Foundation, the U.S. Department of Energy, the Japanese Monbukagakusho, and the Max Planck Society. The SDSS website is http://www.sdss.org/.

The SDSS is managed by the Astrophysical Research Consortium (ARC) for the Participating Institutions. The Participating Institutions are the University of Chicago, Fermilab, the Institute for Advanced Study, the Japan Participation Group, Johns Hopkins University, Los Alamos National Laboratory, the Max-Planck-Institute for Astronomy

(MPIA), the Max-Planck-Institute for Astrophysics (MPA), New Mexico State University, University of Pittsburgh, Princeton University, the United States Naval Observatory, and the University of Washington.

Appendix A
Rest-frame Spectra and Fits

The spectral analysis of the 13 objects of our sample is shown in Figure 16.

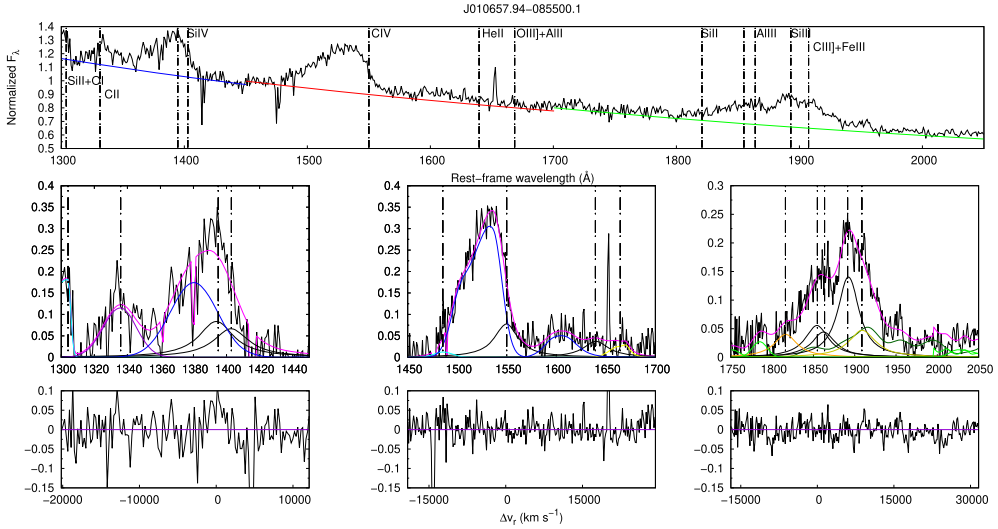

Figure 16. (a) Top panels: calibrated rest-frame spectrum of SDSS J010657.94−085500.1 before continuum subtraction. Global or local continuum is specified by a solid colored line, while the black line marks rest-framed data. Dotted–dashed vertical lines correspond to the rest-frame wavelength of each emission line. Bottom: multicomponent fits after continuum subtraction for the Si IV λ1397, C IV λ1549, and λ1900 blend spectral ranges. The solid black line marks the BC at rest frame associated with Si IV λ1397, C IV λ1549, and Al III λ1860; the blue one marks the blueshifted component associated with each emission. The magenta line corresponds to the fit to the whole spectrum. In the bottom left panel, the light-blue line marks the contribution of the O I + S II λ1304 blend, while the violet line corresponds to the C II λ1335 emission line. In the C IV λ1549 region, N IV] λ1486 is represented by a light-blue line, while the gold one corresponds to the O III] λ1663 + Al II λ1670 blend. In the λ1900 blend range, Fe III and Fe II contributions are marked by dark- and light-green lines, respectively. Violet lines mark the N III] λ1750 line, the orange one corresponds to the S III λ1816 line, and the gold one corresponds to the C III] λ1909 line. Lower panels correspond to the residuals, in radial velocity units km s^{-1} and in Å. (b) Same as the previous panel, but for SDSS J082936.30+080140.6, SDSS J084525.84+072222.3, and SDSS J084719.12 +094323.4. (c) Same as the previous panel, but for SDSS J085856.00+015219.4, SDSS J092641.41+013506.6, and SDSS J094637.83−012411.5. (d) Same as previous panel, but for SDSS J102421.32+024520.2, SDSS J102606.67+011459.0, and SDSS J114557.84+080029.0. (e) Same as the previous panel, but for SDSS J150959.16+074450.1, SDSS J151929.45+072328.7, and SDSS J211651.48+044123.7.

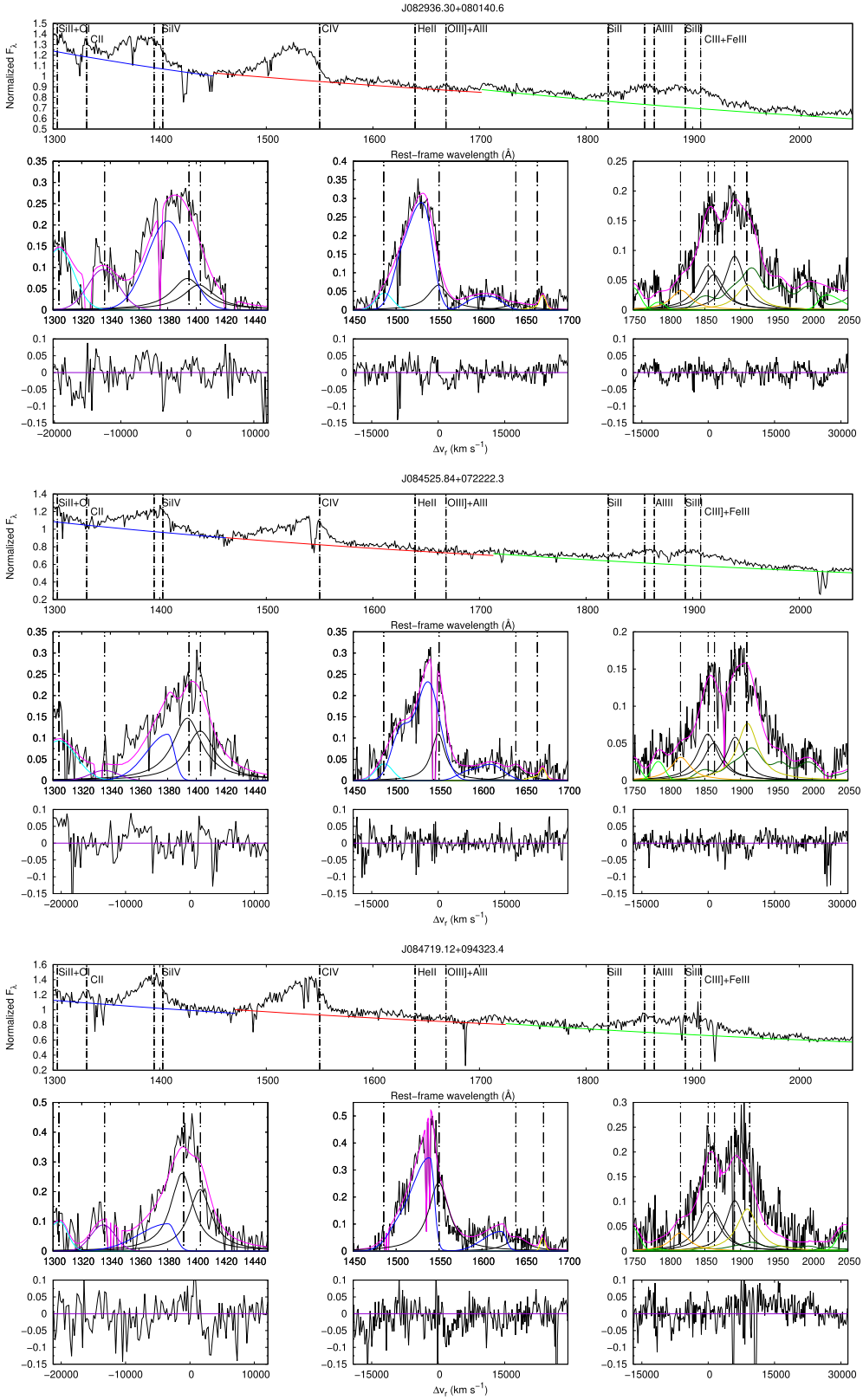

Figure 16. (Continued.)

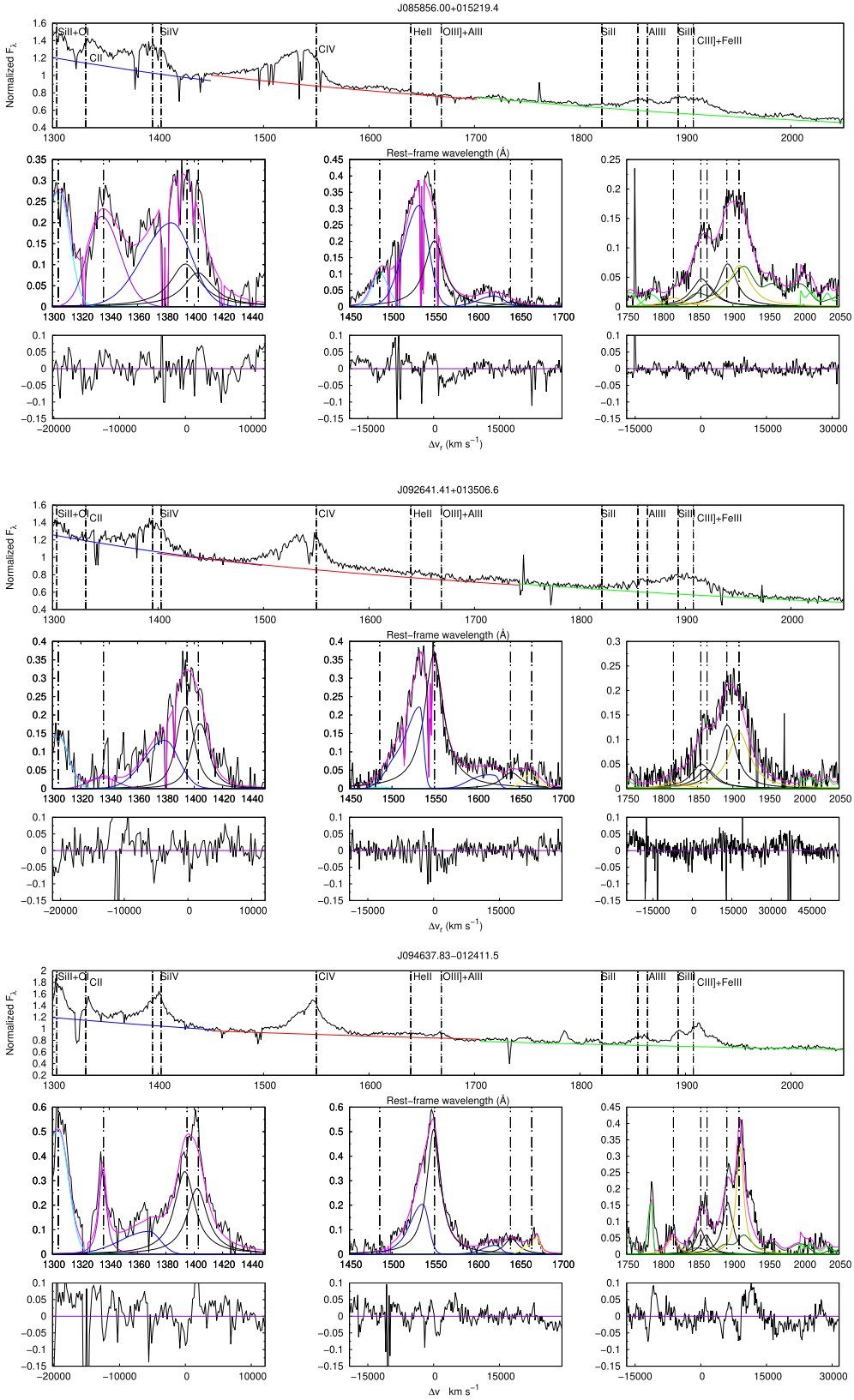

Figure 16. (Continued.)

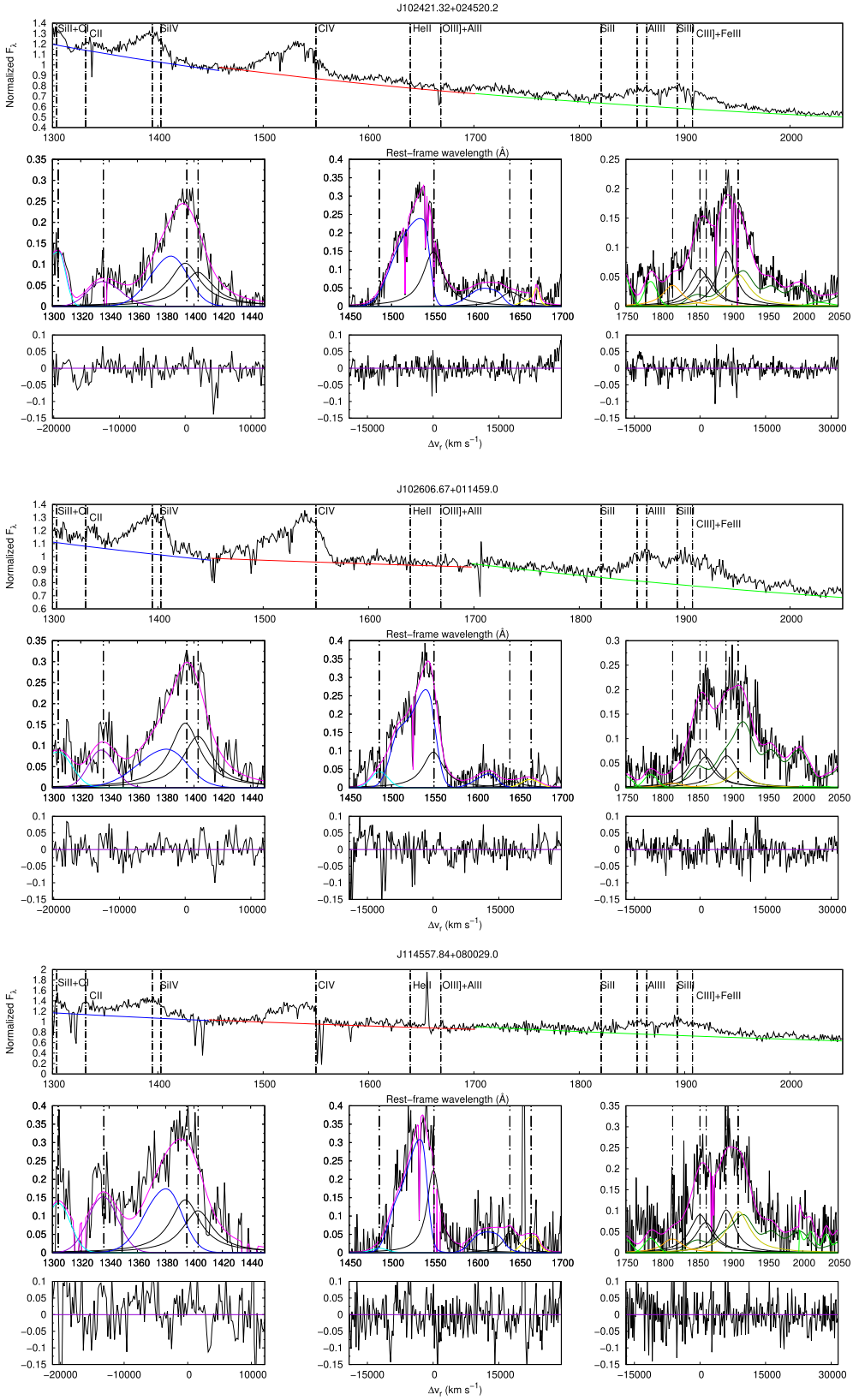

Figure 16. (Continued.)

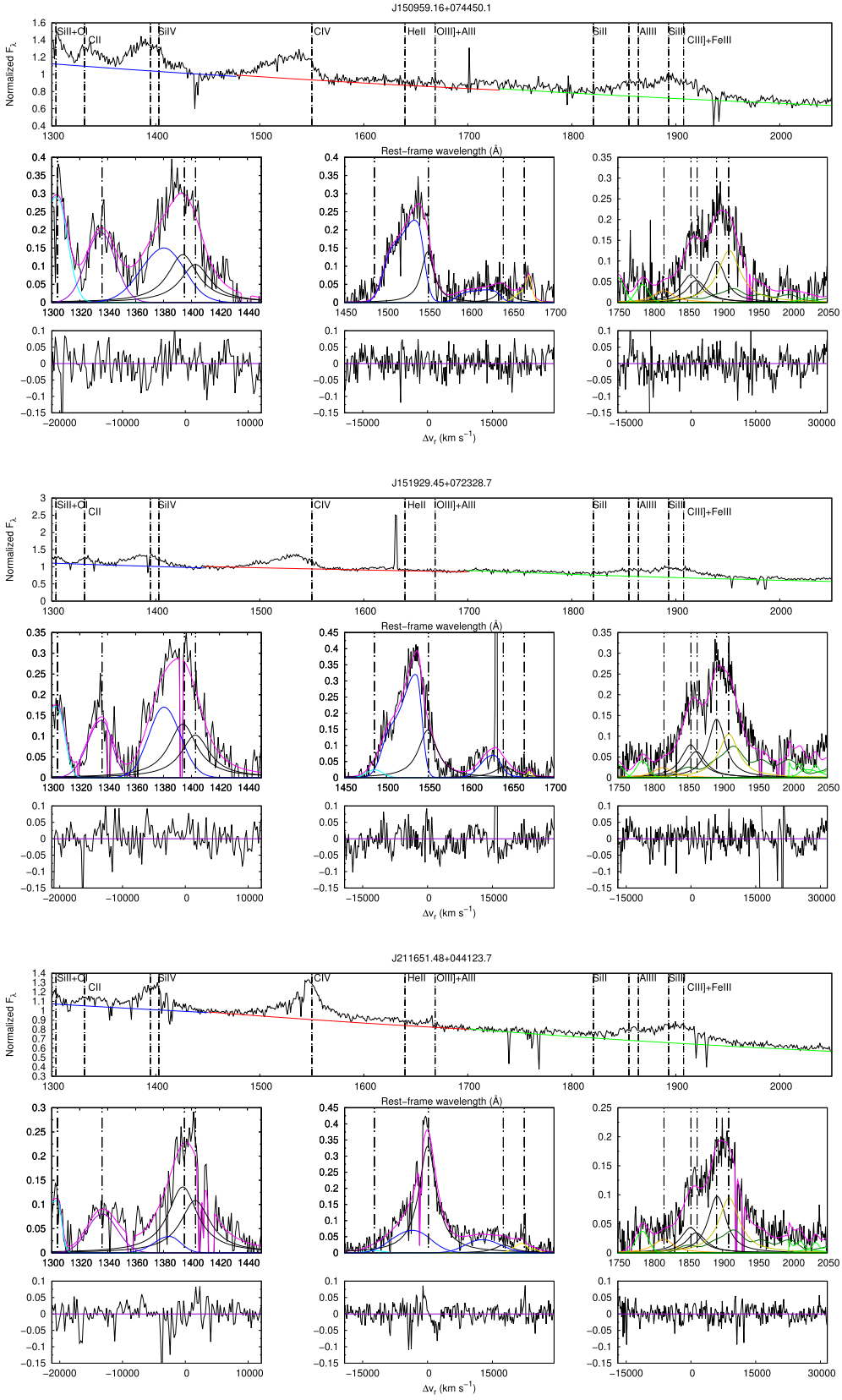

Figure 16. (Continued.)

Appendix B
Diagnostic Intensity Ratios in the Plane (U, $n_{\rm H}$) as a Function of Metallicity

The results of the arrays of simulations as a function of $n_{\rm H}$, U, and Z are shown in Figures 17 and 18, for $N_{\rm c} = 10^{23}$. The SED shape is the same for all simulations (table_agn), which corresponds to the SED of Mathews & Ferland (1987). No turbulence was assumed.

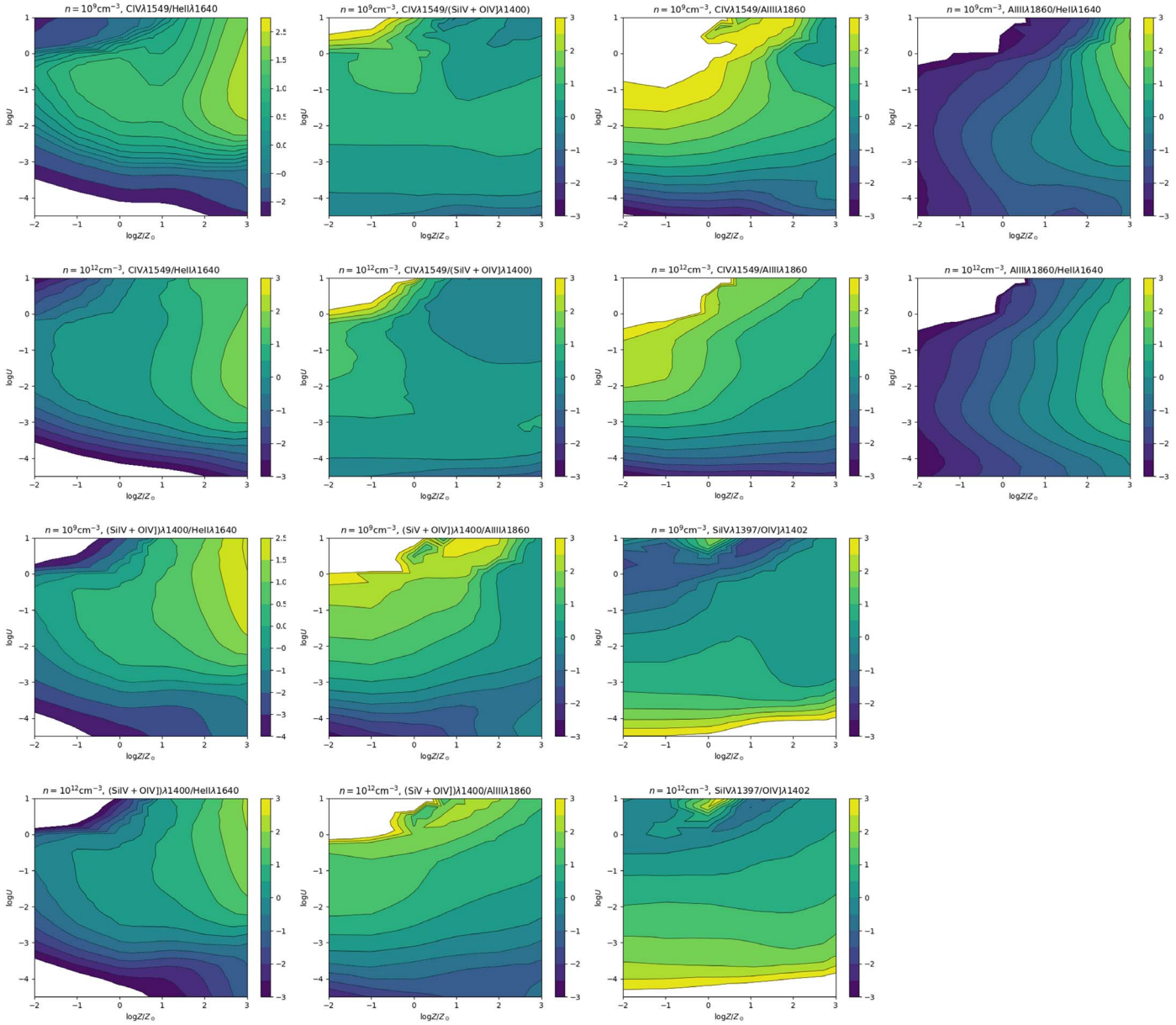

Figure 17. Isophotal contour in the $\log U$–$\log Z$ plane of seven diagnostic line intensity ratios, computed assuming column density $N_{\rm c} = 10^{23}$ cm^{-2}. Top rows, from left to right: logarithm of C IV/He II, C IV/(Si IV + O IV]), C IV/Al III, Al III/He II λ1640. Bottom rows, from left to right: logarithm of (Si IV + O IV])/He II, (Si IV + O IV])/Al III, Si IV/O IV]. The contour plots are shown for $n_{\rm H} = 10^9$ cm^{-3} (top) and $n_{\rm H} = 10^{12}$ cm^{-3} (bottom) for each diagnostic ratio.

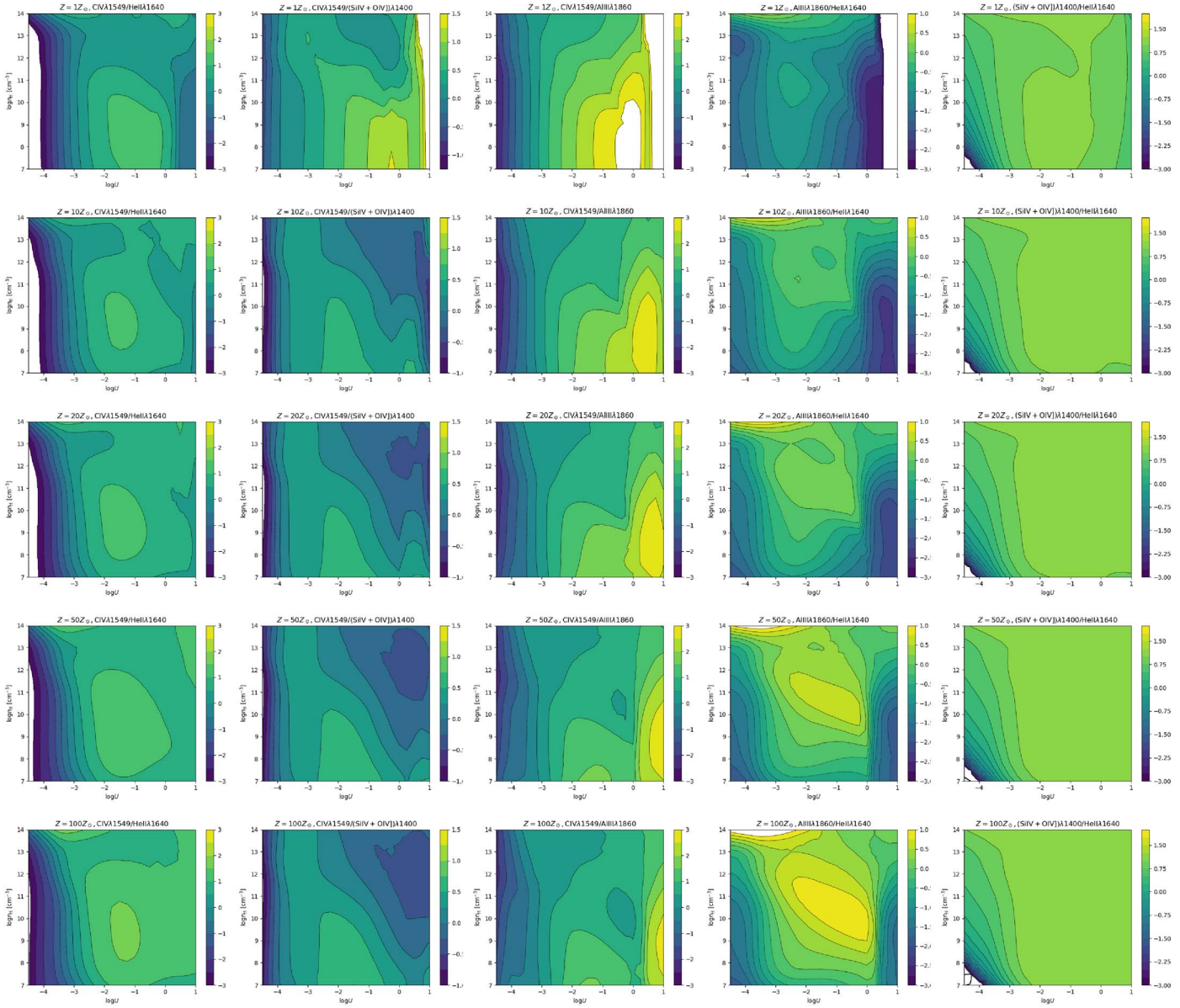

Figure 18. Isophotal contour in the $\log U$–$\log n_{\rm H}$ for line intensity ratios (from left to right) C IV/He II, C IV/(Si IV + O IV]), C IV/Al III, Al III/He II λ1640, (Si IV + O IV])/He II λ1640) as a function of metallicity (from top to bottom: $Z = 1$, 10, 20, 50, 100 $Z_{\odot}$), for column density $N_{\rm c} = 10^{23}$ cm^{-2}.

ORCID iDs

Marzena Śniegowska https://orcid.org/0000-0003-2656-6726
Paola Marziani https://orcid.org/0000-0002-6058-4912
Bożena Czerny https://orcid.org/0000-0001-5848-4333
Swayamtrupta Panda https://orcid.org/0000-0002-5854-7426
Mary Loli Martínez-Aldama https://orcid.org/0000-0002-7843-7689
Ascensión del Olmo https://orcid.org/0000-0003-2055-9816
Mauro D'Onofrio https://orcid.org/0000-0001-6441-9044

References

Abramowicz, M. A., Czerny, B., Lasota, J. P., & Szuszkiewicz, E. 1988, ApJ, 332, 646
Adelman-McCarthy, J. K., Agüeros, M. A., Allam, S. S., et al. 2008, ApJS, 175, 297
Adhikari, T. P., Różańska, A., Czerny, B., Hryniewicz, K., & Ferland, G. J. 2016, ApJ, 831, 68
Anders, E., & Grevesse, N. 1989, Geochim. Cosmochim. Acta, 53, 197
Baldwin, J. A., Hamann, F., Korista, K. T., et al. 2003, ApJ, 583, 649
Bañados, E., Venemans, B. P., Decarli, R., et al. 2016, ApJS, 227, 11
Baskin, A., & Laor, A. 2012, MNRAS, 426, 1144
Becker, R. H., White, R. L., & Helfand, D. J. 1995, ApJ, 450, 559
Bevington, P. R., & Robinson, D. K. 2003, Data Reduction and Error Analysis for the Physical Sciences (Boston, MA: McGraw-Hill)
Bisogni, S., di Serego Alighieri, S., Goldoni, P., et al. 2017, A&A, 603, A1
Boroson, T. A., & Green, R. F. 1992, ApJS, 80, 109
Brotherton, M. S., Wills, B. J., Francis, P. J., & Steidel, C. C. 1994, ApJ, 430, 495
Brühweiler, F., & Verner, E. 2008, ApJ, 675, 83
Cantiello, M., Jermyn, A. S., & Lin, D. N. C. 2020, arXiv:2009.03936
Chieffi, A., & Limongi, M. 2013, ApJ, 764, 21
Coatman, L., Hewett, P. C., Banerji, M., & Richards, G. T. 2016, MNRAS, 461, 647
Collin, S., & Zahn, J.-P. 1999a, A&A, 344, 433
Collin, S., & Zahn, J.-P. 1999b, Ap&SS, 265, 501
Collin-Souffrin, S., Dyson, J. E., McDowell, J. C., & Perry, J. J. 1988, MNRAS, 232, 539
Collin-Souffrin, S., & Lasota, J.-P. 1988, PASP, 100, 1041
Corbin, M. R., & Boroson, T. A. 1996, ApJS, 107, 69

D' Agostini, G. 2003, Bayesian Reasoning in Data Analysis—A Critical Introduction (Singapore: World Scientific)
Davidson, K., & Netzer, H. 1979, RvMP, 51, 715
Diamond-Stanic, A. M., Fan, X., Brandt, W. N., et al. 2009, ApJ, 699, 782
Dietrich, M., Hamann, F., Shields, J. C., et al. 2003, ApJ, 589, 722
D'Onofrio, M., & Marziani, P. 2018, FrASS, 5, 31
Du, P., Lu, K.-X., Hu, C., et al. 2016a, ApJ, 820, 27
Du, P., Wang, J.-M., Hu, C., et al. 2014, MNRAS, 438, 2828
Du, P., Wang, J.-M., Hu, C., et al. 2016b, ApJL, 818, L14
Elvis, M. 2000, ApJ, 545, 63
Feibelman, W. A., & Aller, L. H. 1987, ApJ, 319, 407
Ferland, G. J., Chatzikos, M., Guzmán, F., et al. 2017, RMxAA, 53, 385
Ferland, G. J., Done, C., Jin, C., Landt, H., & Ward, M. J. 2020, MNRAS, 494, 5917
Ferland, G. J., Hu, C., Wang, J., et al. 2009, ApJL, 707, L82
Ferland, G. J., Porter, R. L., van Hoof, P. A. M., et al. 2013, RMxAA, 49, 137
Gaskell, C. M. 2000, NewAR, 44, 563
Graham, M. J., Clowes, R. G., & Campusano, L. E. 1996, MNRAS, 279, 1349
Grevesse, N., & Sauval, A. J. 1998, SSRv, 85, 161
Hamann, F., & Ferland, G. 1992, ApJL, 391, L53
Hamann, F., & Ferland, G. 1999, ARA&A, 37, 487
Hamann, F., Korista, K. T., Ferland, G. J., Warner, C., & Baldwin, J. 2002, ApJ, 564, 592
Hartig, G. F., & Baldwin, J. A. 1986, ApJ, 302, 64
Izotov, Y. I., & Thuan, T. X. 1999, ApJ, 511, 639
Juarez, Y., Maiolino, R., Mujica, R., et al. 2009, A&A, 494, L25
Kaspi, S., Brandt, W. N., Maoz, D., et al. 2007, ApJ, 659, 997
Keenan, F. P., Ahmed, S., Brage, T., et al. 2002, MNRAS, 337, 901
Kovačević-Dojčinović, J., & Popović, L. Č. 2015, ApJS, 221, 35
Kriss, G. 1994, in ASP Conf. Ser. 61, Astronomical Data Analysis Software and Systems III, ed. D. R. Crabtree, R. J. Hanisch, & J. Barnes (San Francisco, CA: ASP), 437
Kuraszkiewicz, J., Wilkes, B. J., Schmidt, G., et al. 2009, ApJ, 692, 1180
Leighly, K. M., & Moore, J. R. 2004, ApJ, 611, 107
Lipari, S., Terlevich, R., & Macchetto, F. 1993, ApJ, 406, 451
Maiolino, R., & Mannucci, F. 2019, A&ARv, 27, 3
Martínez-Aldama, M. L., Del Olmo, A., Marziani, P., et al. 2017, FrASS, 4, 29
Martínez-Aldama, M. L., del Olmo, A., Marziani, P., et al. 2018a, A&A, 618, A179
Martínez-Aldama, M. L., Del Olmo, A., Marziani, P., et al. 2018b, FrASS, 4, 65
Marziani, P., del Olmo, A., Perea, J., D'Onofrio, M., & Panda, S. 2020, Atoms, 8, 94
Marziani, P., Dultzin, D., Sulentic, J. W., et al. 2018, FrASS, 5, 6
Marziani, P., Martínez Carballo, M. A., Sulentic, J. W., et al. 2016a, Ap&SS, 361, 29
Marziani, P., & Sulentic, J. W. 2014, MNRAS, 442, 1211
Marziani, P., Sulentic, J. W., Dultzin-Hacyan, D., Calvani, M., & Moles, M. 1996, ApJS, 104, 37
Marziani, P., Sulentic, J. W., Negrete, C. A., et al. 2010, MNRAS, 409, 1033
Marziani, P., Sulentic, J. W., Stirpe, G. M., et al. 2016b, Ap&SS, 361, 3
Marziani, P., Sulentic, J. W., Stirpe, G. M., Zamfir, S., & Calvani, M. 2009, A&A, 495, 83
Mathews, W. G., & Ferland, G. J. 1987, ApJ, 323, 456
Mathur, S. 2000, MNRAS, 314, L17
Matsuoka, K., Nagao, T., Marconi, A., Maiolino, R., & Taniguchi, Y. 2011, A&A, 527, A100
Matsuoka, Y., Oyabu, S., Tsuzuki, Y., & Kawara, K. 2007, ApJ, 663, 781
Matthews, J. H. 2016, PhD thesis, Univ. Southampton
Mejía-Restrepo, J. E., Trakhtenbrot, B., Lira, P., Netzer, H., & Capellupo, D. M. 2016, MNRAS, 460, 187
Murray, N., & Chiang, J. 1997, ApJ, 474, 91
Murray, N., Chiang, J., Grossman, S. A., & Voit, G. M. 1995, ApJ, 451, 498
Nagao, T., Maiolino, R., & Marconi, A. 2006a, A&A, 447, 863
Nagao, T., Marconi, A., & Maiolino, R. 2006b, A&A, 447, 157
Nardini, E., Lusso, E., Risaliti, G., et al. 2019, A&A, 632, A109
Negrete, A., Dultzin, D., Marziani, P., & Sulentic, J. 2012, ApJ, 757, 62
Negrete, C. A., Dultzin, D., Marziani, P., et al. 2018, A&A, 620, A118
Negrete, C. A., Dultzin, D., Marziani, P., & Sulentic, J. 2010, arXiv:1011.4248
Negrete, C. A., Dultzin, D., Marziani, P., & Sulentic, J. W. 2014, ApJ, 794, 95
Netzer, H., & Marziani, P. 2010, ApJ, 724, 318
Onoue, M., Bañados, E., Mazzucchelli, C., et al. 2020, ApJ, 898, 105
Osmer, P. S., & Smith, M. G. 1976, ApJ, 210, 267
Osterbrock, D. E., & Ferland, G. J. 2006, Astrophysics of Gaseous Nebulae and Active Galactic Nuclei (Mill Valley, CA: Univ. Science Books)
Osterbrock, D. E., & Pogge, R. W. 1985, ApJ, 297, 166
Panda, S. 2020, arXiv:2004.13113
Panda, S., Czerny, B., Adhikari, T. P., et al. 2018, ApJ, 866, 115
Panda, S., Martínez-Aldama, M. L., Marinello, M., et al. 2020a, ApJ, 902, 76
Panda, S., Marziani, P., & Czerny, B. 2019, ApJ, 882, 79
Panda, S., Marziani, P., & Czerny, B. 2020b, CoSka, 50, 293
Pâris, I., Petitjean, P., Ross, N. P., et al. 2017, A&A, 597, A79
Peimbert, A., Peimbert, M., & Luridiana, V. 2001, RMxAC, 10, 148
Peimbert, M. 2008, arXiv:0811.2980
Peterson, B. M., & Wandel, A. 1999, ApJL, 521, L95
Plotkin, R. M., Shemmer, O., Trakhtenbrot, B., et al. 2015, ApJ, 805, 123
Popović, L. Č., Mediavilla, E. G., Kubičela, A., & Jovanović, P. 2002, A&A, 390, 473
Proga, D. 2007a, ApJ, 661, 693
Proga, D. 2007b, in ASP Conf. Ser. 373, The Central Engine of Active Galactic Nuclei, ed. L. C. Ho & J.-W. Wang (San Francisco, CA: ASP), 267
Punsly, B., Marziani, P., Bennert, V. N., Nagai, H., & Gurwell, M. A. 2018, ApJ, 869, 143
Richards, G. T., Kruczek, N. E., Gallagher, S. C., et al. 2011, AJ, 141, 167
Richards, G. T., Lacy, M., Storrie-Lombardi, L. J., et al. 2006, ApJS, 166, 470
Risaliti, G., & Elvis, M. 2010, A&A, 516, A89
Risaliti, G., Salvati, M., & Marconi, A. 2011, MNRAS, 411, 2223
Sądowski, A., Narayan, R., McKinney, J. C., & Tchekhovskoy, A. 2014, MNRAS, 439, 503
Schneider, D. P., Richards, G. T., Hall, P. B., et al. 2010, AJ, 139, 2360
Shemmer, O., & Netzer, H. 2002, ApJL, 567, L19
Shemmer, O., Netzer, H., Maiolino, R., et al. 2004, ApJ, 614, 547
Shen, Y. 2016, ApJ, 817, 55
Shen, Y., & Ho, L. C. 2014, Natur, 513, 210
Shen, Y., Richards, G. T., Strauss, M. A., et al. 2011, ApJS, 194, 45
Shields, G. A. 1976, ApJ, 204, 330
Shin, J., Nagao, T., & Woo, J.-H. 2017, ApJ, 835, 24
Shin, J., Woo, J.-H., Nagao, T., & Kim, S. C. 2013, ApJ, 763, 58
Sulentic, J. W., Bachev, R., Marziani, P., Negrete, C. A., & Dultzin, D. 2007, ApJ, 666, 757
Sulentic, J. W., del Olmo, A., Marziani, P., et al. 2017, A&A, 608, A122
Sulentic, J. W., Marziani, P., del Olmo, A., et al. 2014, A&A, 570, A96
Sulentic, J. W., Marziani, P., & Dultzin-Hacyan, D. 2000a, ARA&A, 38, 521
Sulentic, J. W., Marziani, P., Dultzin-Hacyan, D., Calvani, M., & Moles, M. 1995, ApJL, 445, L85
Sulentic, J. W., Marziani, P., Zamanov, R., et al. 2002, ApJL, 566, L71
Sulentic, J. W., Repetto, P., Stirpe, G. M., et al. 2006, A&A, 456, 929
Sulentic, J. W., Zwitter, T., Marziani, P., & Dultzin-Hacyan, D. 2000b, ApJL, 536, L5
Szuszkiewicz, E., Malkan, M. A., & Abramowicz, M. A. 1996, ApJ, 458, 474
Temple, M. J., Ferland, G. J., Rankine, A. L., et al. 2020, MNRAS, 496, 2565
Vanden Berk, D. E., Richards, G. T., Bauer, A., et al. 2001, AJ, 122, 549
Verner, E. M., Verner, D. A., Korista, K. T., et al. 1999, ApJS, 120, 101
Véron-Cetty, M.-P., Véron, P., & Gonçalves, A. C. 2001, A&A, 372, 730
Vestergaard, M., & Peterson, B. M. 2006, ApJ, 641, 689
Vestergaard, M., & Wilkes, B. J. 2001, ApJS, 134, 1
Vietri, G., Piconcelli, E., Bischetti, M., et al. 2018, A&A, 617, A81
Vila-Costas, M. B., & Edmunds, M. G. 1993, MNRAS, 265, 199
Wang, H., Zhou, H., Yuan, W., & Wang, T. 2012a, ApJL, 751, L23
Wang, J.-M., Du, P., Baldwin, J. A., et al. 2012b, ApJ, 746, 137
Wang, J.-M., Du, P., Li, Y.-R., et al. 2014, ApJL, 792, L13
Wang, J.-M., Du, P., Valls-Gabaud, D., Hu, C., & Netzer, H. 2013, PhRvL, 110, 081301
Wang, J.-M., Ge, J.-Q., Hu, C., et al. 2011, ApJ, 739, 3
Warner, C., Hamann, F., & Dietrich, M. 2004, ApJ, 608, 136
Welch, B. L. 1947, Biometrika, 34, 28
Wildy, C., Czerny, B., & Panda, S. 2019, A&A, 632, A41
Wills, D., & Netzer, H. 1979, ApJ, 233, 1
Xu, D., Komossa, S., Zhou, H., et al. 2012, AJ, 143, 83
Xu, X., Zakamska, N. L., Arav, N., Miller, T., & Benn, C. 2020, MNRAS, 495, 305
Zamanov, R., Marziani, P., Sulentic, J. W., et al. 2002, ApJL, 576, L9
Zheng, W. 1988, ApL&C, 27, 275
Zhou, H., Wang, T., Yuan, W., et al. 2006, ApJS, 166, 128